

Neutral Hydrogen Filaments in interstellar media: Are they physical?

Ka Ho Yuen^{1*}, Ka Wai Ho^{1,2}, Chi Yan Law³ and Avi Chen⁴

^{1*}Theoretical Division, Los Alamos National Laboratory, Los Alamos, 87545, NM, USA.

²Department of Astronomy, University of Wisconsin-Madison, 454 N. Charter St, Madison, 53715, WI, USA.

³Department of Space, Earth & Environment, Chalmers University of Technology, SE-412 96, Gothenburg, Sweden.

⁴ Department of Physics and Astronomy, Rutgers University, 136 Frelinghuysen Rd, Piscataway, 08854, NJ, USA.

*Corresponding author(s). E-mail(s): kyuen@lanl.gov;

Abstract

The trending term "filament" is extensively used in the interstellar medium (ISM) and the star formation community, and is believed to be one of the most important objects that gauge molecular cloud and star formation. However, the physical definition of these ubiquitous, elongated, high contrast features is poorly defined and still actively debated. Despite the absence of a unified consensus, filaments are believed to be involved in many important physical processes from galaxy structure formation to the emergence of protostellar objects. Therefore, understanding how filaments form, what constrains their growth, and their general physical properties, are extremely important for theorists and observers who study the dynamics of the ISM and consequent star formations. This review serves as a collection of the community's views and develops the concept of "filaments" in the context of the ISM and star-forming clouds. Observationally, filaments are seen across the entire sky and often carry an aspect ratio of the order of hundreds. In the context of the ISM, filaments are believed to form by stretching and tearing from magnetized ISM turbulence. ISM filaments are subjected to heating and cooling phases, and are likely to be magnetically aligned. Cold clouds are formed inside ISM due to turbulence instability. This review updates the understanding of ISM filaments in the community.

Keywords: Interstellar Media, Magnetic Field, Filaments, Star Formation, Turbulence

1 Overview: What are "filaments" in the context of ISM?

Since early astronomical observations of the 'dark lane' that stands out in the sky in contrast to the bright galactic background, which is opaque in visible to near-infrared wavelengths, filamentary structures have been presented across the different phases of the interstellar medium across a wide range of scales from kilo-parsec to sub-parsec scales (See [McClure-Griffiths et al 2023](#) for a review). These structures are elongated features that have an aspect ratio significantly larger than unity and are an essential component in our understanding of the formation and evolution of stars, star clusters and Galaxies.

The atomic hydrogen cold neutral medium (HI-CNM) is a popular and important astrophysical observable. Observations like HI4PI ([Kalberla and Haud, 2015a](#)), GALFA ([Peek et al, 2018](#)), THOR-HI ([Bialy and Sternberg, 2016](#)), and FAST (e.g. [Yuen et al 2023a](#)) have advanced our understanding of CNM, including its spatial distribution ([Kalberla and Haud, 2018](#)), its relation to magnetic fields ([Heiles and Troland, 2003](#); [Clark et al, 2015](#)), and its connection to the underlying molecular phase ([Kritsuk et al, 2017](#)). CNM is ubiquitous in the interstellar medium (ISM), spanning from high latitude ([Clark et al, 2015](#)) to the galactic plane ([Soler et al, 2020](#)), and is highly filamentary with filaments aligned along the magnetic field direction ([Clark et al, 2015](#); [Yuen and Lazarian, 2017b](#)). This feature of CNM makes it one of the most important B-field probes in modern astronomy, with vast applications from cosmology ([Clark et al, 2019](#)) to diffuse molecular cloud studies (e.g., [Lazarian and Yuen 2018b](#)). The nature of CNM is also very important in understanding the formation of molecular clouds. With a density of 10cm^{-3} or higher the CNM is already near the critical density for H₂ formation (50cm^{-3}). Due to the rapid conversion between HI and H₂ ([Bialy and Sternberg, 2016](#)), the formed CNM can quickly convert into molecular hydrogen and experience Jeans instability, leading to the formation of molecular clouds.

While filamentary structures are expected to play a crucial role in structure formation and evolution in the ISM, many open questions remain. We list a few of these questions, which motivate and form the backbone of this review.

1.1 Why are observed CNM filaments in the ISM only parallel to B-field while simulations contain both parallel and perpendicular?

Our understanding of the physics of the multiphase is rather limited and hasn't advanced much from the description of the two-phase model of neutral media proposed in the late 20th century ([McKee and Ostriker 1977](#), left of Fig 2). The ISM in our Milky Way galaxy is threaded by ubiquitous turbulent magnetic fields. This was realized long ago. For instance, in the 2004 ARA&A review, [Scalo and Elmegreen \(2004\)](#) wrote: "*One of the most important developments*

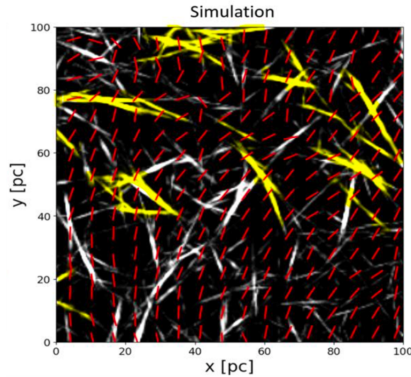


Fig. 1 Extracted filaments using Rolling Hough Transform (RHT) in multiphase numerical simulation from [Kritsuk et al \(2017\)](#) (Credits: A. Kritsuk). The underlying vectors for both figures are the magnetic field directions in their retrospectives. We highlight the parallel filaments (filaments that are parallel to B-field) as white, the perpendicular filaments (filaments that are perpendicular to B-field) as yellow on the RHS to illustrate the differences between observations and simulations: There are almost no perpendicular filaments in observed HI data, but a vast number of filaments in simulations are perpendicular to B.

in the field of interstellar gas ...was that ... most processes and structures are strongly affected by turbulence”.

The ubiquity and linearity of CNM can best be explained with MHD turbulence theory. Filamentary features are mainly formed by: (1) low-density fluctuations along the magnetic field and (2) high-density shock compression perpendicular to the magnetic field. Isothermal numerical simulations ([Kowal et al, 2007](#); [Kowal and Lazarian, 2010](#); [Kim and Ostriker, 2018](#); [Lazarian and Yuen, 2018b](#)) suggest that CNM filaments form both parallel and perpendicular to the magnetic field (Fig. 1). The number of parallel and perpendicular filaments have a comparable population in simulations, but it does not seem to be the case in observations (See, e.g. [Clark et al \(2015\)](#); [Syed et al \(2022\)](#)).

Most HI linear features that are proposed candidates of CNM ([Clark et al, 2019](#)), are preferentially parallel to the magnetic field ([Clark et al 2014, 2015](#)). Only in very rare circumstances do we observe CNM perpendicular to the magnetic field ([Kritsuk et al, 2017](#); [Kim and Ostriker, 2018](#)). A major scientific question regarding CNM candidate is: why are filaments exclusively parallel to magnetic fields in observations and not in numerical simulations? (See Fig 1.)

1.2 Why is the aspect ratio of observed CNM in the hundreds while in simulations they are not?

The observed parallel HI filaments generally have a very high aspect ratio, ranging from 30 to 100 (see Tab. 2) and are suggested to be associated with cold features ([Clark et al, 2019](#)). Given the ubiquity of these long, cold, and thin filaments across the full sky (~ 0.1 pc thick, [Kalberla et al 2021](#)), there must be a universal mechanism favoring the formation of such long CNM structures. One of the most common explanations is the equally ubiquitous magnetized

turbulence, shaping the multiphase media according to the Goldreich-Sridhar scaling (hereafter GS95) (Goldreich and Sridhar 1995, see also Lazarian and Vishniac 1999; Xu et al 2019). This scaling predicts that filaments in isothermal MHD turbulence should scale as $l_{\parallel}/l_{\perp} \sim M_A^{-4/3} (L_{inj}/l_{\perp})^{1/3}$. However, the observed filaments are much longer than this prediction when realistic values of the Alfvénic Mach number M_A , turbulence injection scale L_{inj} , and thickness l_{\perp} of cold neutral media are considered (green line in Fig. 3). Another recently proposed mechanism favoring the formation of long filaments is small-scale reconnection (Kalberla et al, 2021). Yet no theoretical models explain how the statistics of the aspect ratio are related to the properties of small-scale reconnection.

Simulations (Ho et al, 2023) have shown that cold filaments formed in multiphase media are considerably shorter in length than what is observed (Fig 3). Even for simulation with adaptive mesh refinement (e.g. Seifried et al 2022), the HI filaments are still much shorter than what we observe in HI maps. The aspect ratios in these simulations is also significantly shorter than what GS95 predicted (Ho et al 2023, Fig 3), suggesting that the formation of long cold filaments may not be solely attributed to the stretching and tearing of magnetized turbulence. This raises the question of whether the GS95 scaling is an appropriate description for modeling the statistics of filament aspect ratios. It is known that the GS95 critical balance does not hold during the UNM stage. Ho et al (2023) suggests that the "cold filaments" identified through observations may not be physically stable and could be subject to a new instability, which naturally breaks down the filaments into clumps with shorter aspect ratios. This prompts us to inquire about the origin of the very long features observed in these observations.

1.3 The main question of this review: Are filaments in the ISM actually physical?

Before addressing the above questions, it would be fruitful to ask a simpler question: **Are the observed filamentary features real or a computational artifacts?** Interpretation of these magnetically aligned, elongated over-dense features is widely discussed in the literature (See Kalberla et al 2021), but understanding the nature of their physical properties, including their origin, stability, and fate, is crucial for comprehending the full physics of multiphase interstellar media, particularly in shaping and controlling the star formation rate in molecular clouds. Furthermore, how the more ambient HI gases at scales of kpc form molecular clouds at pcs, and subsequently stars in sub-pcs, remains an open question for the community.

Readers should note that while this review attempts to be as comprehensive as possible, the analysis of filaments has rapidly evolved since the renowned filament review by André et al (2014). Machine learning vision algorithms are much more powerful in 2024 than they were in 2014. We will include as many important results as possible up to the authors' knowledge, with essential ideas covered and extended literature for readers to follow up.

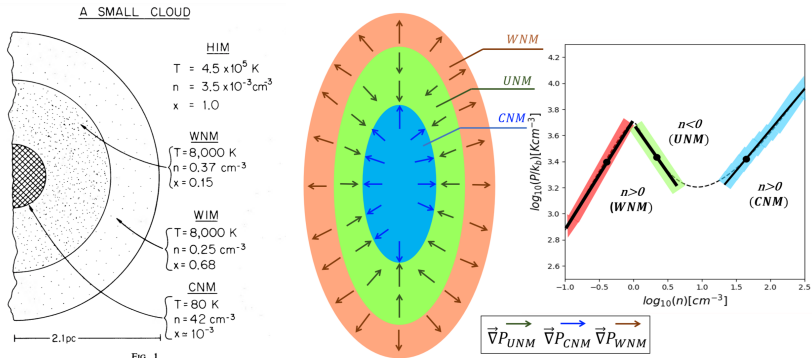


Fig. 2 Illustration of the Multiphase model. Left: Model from [McKee and Ostriker \(1977\)](#). In their model, they only recognize two phases in the neutral stage, namely the warm neutral media (WNM) and cold neutral media (CNM). Middle and right panels: Modern understanding of the multiphase model and the respective phase diagram. From the phase diagram (right panel), we can identify three separate phases (middle panel). The new unstable phase, unstable neutral media (UNM), possesses a very special property: (1) it is a transient phase and in unstable equilibrium, i.e., the adiabatic index $n < 0$. (2) the pressure force exerted by UNM is attractive (green vectors in the middle panel). If we consider the pressure balances between the phases, the contracting pressure force from UNM (middle) is counterbalanced by the repelling force from the CNM. This force balance limits the length of the CNM ([Ho et al, 2023](#)).

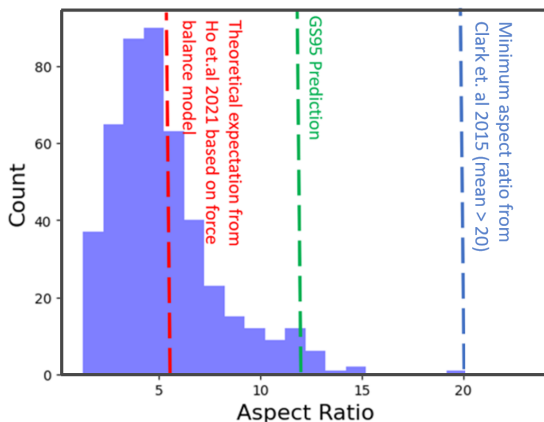


Fig. 3 The aspect ratio distribution of filamentary structure from multi-phase simulation ([Ho et al, 2023](#)), with the prediction from GS95 (green line), the measured ratio by the RHT technique (blue line, [Clark et al \(2014\)](#)), and the prediction including the effect from UNM (red line, [Ho et al \(2023\)](#)). It is therefore postulated that the elongated features in the sky are not real CNM and are not governed by GS95.

2 Filament identification and characteristic: An observational perspective

A key aspect of this review is to provide readers with the limitations of and caveats on characterising properties of filaments from observations (or more formally, a projected image from telescope observations) to infer the underlying physics, in which to compare with the output of simulations with a certain recipe that contains certain fundamental physics. To answer the central questions outlined in the previous sections demands a review of the state of the art in the identification methods of 'filamentary' structures in the heavens and the underlying inferred physics. Despite this review focusing on CNM filament, one of the tensions in comparing observations and simulation finds, independent of the interstellar phase of converters, is that the physical quantities reported from observational studies are structured 'post-processed' by certain methods that may already involve a certain underlying restriction on the meaning of 'filament' and the corresponding physics. However, simulations studied mainly concern reviewing the physics and do not normally take care of observational properties such as instrumentation artefacts, noise properties, and post-process methods, which could contaminate or even alter the resulting products, which led to an unfair comparison. In Section 2.1, we first review and classify different classes of filament identification approaches and what kind of properties these observed 'filaments' connect to the underlying physics. We then review important observational findings toward 'filaments' in the CNM. Here, we refer the reader to chapters from PPVI by Andre and Li and a chapter by Henshaw in PPVII for focused studies of the observational findings on filaments in the molecular clouds (i.e., molecular hydrogen-dominated phase). In particular, we review certain key observational metrics, such as the autocorrelation function, reduction factors (a.k.a alignment measures), model fitting to the radial density profile, and power spectrum, and their connection to the physics they result in such quantities. While this review focuses on reviewing the fundamental regulating physics of structure formation and evolution in the multi-phase interstellar medium, a particular frontier in the aspect is the magnetic imprint on the gas kinematics and opens up a window to probe the interactions between two regulating mechanisms: magnetic field and turbulence. Filaments are in the spotlight as these commonly seen elongated structures or 'dark lanes' extending from the galactic plane are products of the interplay between the magnetic field and turbulence. Hence, the observed magnetic field properties in CNM provide important information. Confront and evaluate the reality of structures identified by different methods, but not without caveat. We see projected quantities from a 3-D universe, in which many underlying physics are complicated with the projection effects. Hence, it is worth reviewing and summarising the state of the art of projection and de-projection algorithms that allow us to have a glimpse of actual interactions. Here, we point the reader to Frontier's review by Thani on the state of probing 3-D magnetic field structures, as here we intend to focus on

the method of converting between 2-D to 3-D, as observations are 2-D images. A spectral line cube is essentially a 2-D map, but also with the line of sight velocities information, which provides extra information for re-projection (see review by Tahani et al. 2022). We end this section by stressing the essential need for synthetic observations and related visualisation as this allows a more realistic comparison between simulations that do not care about observational limitations but allows evaluation of the impact of observation parameters on the underlying observables or metrics that are the 'bridges' between theories, which is the main focus of next section the corresponding defining observables. Our goal is to articulate the current state in bridging observations and theories (via predictions based from simulation studies), and to address certain important aspects in order to make progresses in understanding the nature of 'filaments' in the CNM. This review is not intended to cover all aspects but to review the current status and identify gaps that require further studies in the next years. we recommend readers to other reviews on similar topics but with different focuses to have a more comprehensive picture of the topic e.g. PPVII chapters by [Hacar et al 2023](#) and [Pineda et al 2023](#)).

2.1 Methods in filament identification

We approach the definition of "filaments" in an astrophysical setting by considering the following set of questions:

1. Are the visual features defined via computer identification algorithms (e.g., Unsharp mask (UNM), Rolling Hough Transform (RHT)) or based on some observational mechanisms (e.g., Velocity caustics)?
2. Are filaments fully continuous, partly discrete, or web-like? Do we expect sub-filaments within filaments?
3. Can projection effects misleadingly make 2D sheet-like structures appear as 1D filaments? (see, e.g., [McKee and Ostriker 2007](#))

Table 1 summarises most of the commonly used algorithms to identify filaments. In Figure 4, we also present some examples of 'filaments' defined by a few of the selected algorithms.

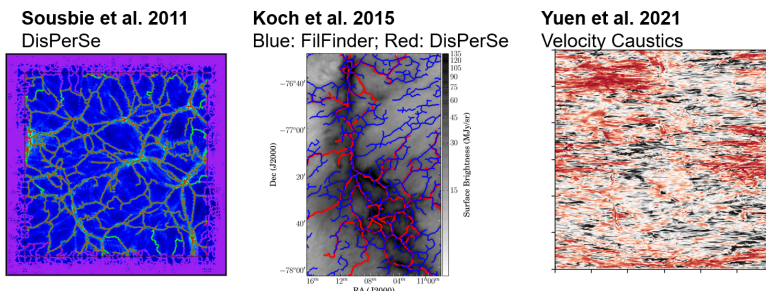


Fig. 4 Filaments identified from selected techniques (See Tab.1). From the left to right : DisPerSe method ([Soubie, 2011](#)), FilFinder ([Koch and Rosolowsky, 2015](#)) and Velocity Caustics Theory ([Yuen et al, 2021](#)). Reproduction of the figures are permitted according to MNRAS guidelines.

Publication	Technique/Algorithm/Package
Rosolowsky et al (2008)	Dendrogram
Sousbie (2011)	DisPerSe
Soler et al (2013)	Intensity Gradient ¹
Clark et al (2014, 2015)	Rolling Hough Transform
Koch and Rosolowsky (2015)	FilFinder
Kalberla et al (2016)	Unsharp Masking
Juvela (2016)	Template matching
González-Casanova and Lazarian (2017)	Velocity Gradient Technique
Soler et al (2020)	Hessian Matrix Technique
Bonnaire et al (2020)	T-ReX
Yuen et al (2021)	Velocity Decomposition Algorithm
Alina et al (2022)	MaLeFiSenta
Xu et al (2023)	CASI-2D

Table 1 Common techniques used in the ISM and star formation community to extract and identify "filaments" in the last decade. See Fig.4 for some of the visualizations.

These methods can be classified into two categories: (i) Image characterisations and (ii) machine learning techniques. Image characterisation techniques are subject to the impact on the intensity map from a given prescription of a real filamentary structure, which could be a dust continuum or an integrated intensity map of a specific molecular species. These prescriptions include continuous yet non-random over-dense regions with a net aspect ratio greater than unity (i.e. the eccentricity of the structure) and distinct start and end-points. This term 'net' is important as it contains an underlying factor that there are reference regions that allow contrast to arise to single out these connected structures. For example, suppose the instrumentation noise is high enough to create a noise 'mask' that makes an integrated intensity map that a 2D uniform distribution could approximate. In that case, the filament will be convoluted with these noises and 'hide' within the 'mask' by losing out the contrast. However, actual observation data involve noises from the instrument and non-related structures. Thus, it is expected to set specific criteria to post confidence in the contract, which could also be known as the signal-to-noise (SNR) technique for filament identifications. These are the fundamental approaches for Dendrogram, Filfinder, and Unsharp Masking. Within this class of methods, a sub-class utilises more subjective approaches via statistical evaluations. For example, one can apply the intensity gradient and look for any continuous signal of contrast (intensity gradient reflects the region with the sharpest slope in the direction intensity profile along a given direction. Other approaches, such as the RHT and the Hessian matrix, are more sophisticated techniques to distill signals from the intensity map, Yuen et al 2019). Despite the wide variety of algorithms available, several common approaches can be summarized, with some illustrative examples listed in Table 1:

A clear caveat of image detection techniques is that it is highly subject to the prescription of a filament imposed on the intensity map: different prescriptions will yield different filaments. Such subjective prescription may be removed via Machine learning (e.g. CASI-2D). Machine learning techniques

have emerged as powerful and time-efficient tools for filament identification by training on data of known filaments based on some criteria or models that implement certain physics (see next section). This can reduce bias compared to methods primarily relying on manual image analysis. However, machine learning models (e.g. [Alina et al 2022](#), [Xu et al 2023](#)) often require training datasets obtained from either observational data or simulations, which the quality of the input data can still limit.

The techniques mentioned above yield outputs that exhibit certain common properties. For instance, the orientation dispersion of filaments is strongly correlated with the Alfvénic Mach number ([Lazarian et al, 2018](#); [Yuen and Lazarian, 2020b](#)). Notably, diffuse, low-density filaments (considered low in density before the $HI-H_2$ transition) tend to align closely with the direction of the magnetic field ([Clark et al, 2015](#); [González-Casanova and Lazarian, 2017](#); [Yuen and Lazarian, 2017b](#)). In the following sections, we will summarize key findings related to the physical properties of HI and molecular cloud filaments. However, as we will discuss in Section 3, it is essential to have a correct theoretical foundation and a proper understanding of the physical nature of filaments when applying these algorithms.

2.2 HI filaments and their relation to MHD turbulence

Filamentary features are ubiquitous in both diffuse interstellar media and dense molecular clouds. Very early observations, both from absorption ([Heiles, 2001](#)) and emission maps ([McClure-Griffiths et al, 2006](#)), seem to indicate that the cold, dense ISM filaments are magnetically aligned. However, it was not until large-scale, high-resolution HI position-position-velocity (PPV) emission data (e.g., *GALFA*, [Peek et al 2018](#)) and line-absorption data (e.g., 21SPONGE, [Murray et al 2018](#)) became available that observers could gain a clear understanding of the turbulence and magnetic properties of cold, dense neutral hydrogen filaments.

The identification of filaments in HI data can usually be performed using three very popular techniques, in the order of their introduction: Rolling Hough Transform (RHT, 2014, [Clark et al 2014](#)), which originated from the idea of particle track tracing in the 1950s and detects linear dense features in two-dimensional maps; Velocity Gradient Technique (VGT, [González-Casanova and Lazarian 2017](#); [Yuen and Lazarian 2017b](#); [Lazarian and Yuen 2018b](#)), which utilizes the first spatial derivative of velocity-related maps (see the first two equations of Eq. 3) to identify features; and Hessian Matrix Method (2019, [Soler et al 2019](#)), which evolved from the Intensity Gradient Method ([Soler et al, 2013](#)) but attempts to perform second-order statistics. Despite employing different methods to identify filaments, these statistical models are all based on the same underlying principle: How **magneto-hydrodynamic turbulence** interacts with thermodynamics.

Despite differences in methodology, a general trend among these methods follows: in the more diffuse interstellar media, the identified filaments are generally aligned with the underlying magnetic field directions ([Heiles and Troland,](#)

Publication	Aspect Ratio	Object
Diffuse ISM		
West et al (2022)	~500	H α from Synchrotron Emission
Clark et al (2014)	~60	Diffuse HI
Li et al (2021)	25 (5kpc), 5 (1kpc)	Cattail
Syed et al (2022)	~ 30	Maggie
Molecular Cloud		
Colombo et al (2021)	8 ~ 26	Molecular clouds from outer galaxy
Kumar et al (2020)	1.2 \pm 0.4	Hub-filament systems from Herschel survey
Leurini et al (2019)	~ 23	G351.776–0.52
Bonne et al (2020)	54	Musa
Jackson et al (2010)	150	Nessie Nebula
Zhang et al (2020a)	4 – 8.4	California

Table 2 Filament aspect ratio from different observations. These selection of examples are non-exclusive.

2003; Clark et al, 2015; González-Casanova and Lazarian, 2017; Yuen and Lazarian, 2017b). When denser clouds are measured, regardless of the phases, they tend to be perpendicular to the magnetic field direction (Soler et al, 2013; Yuen and Lazarian, 2017a). Molecular cloud filaments will be discussed in the next section, and below, we shall delve into the turbulence aspect of the diffuse HI.

Diffuse interstellar media are known to be multiphase (McKee and Ostriker, 1977; Kritsuk et al, 2017), magnetized (Heiles, 2001), and turbulent (Chepurnov and Lazarian, 2010; Yuen et al, 2022). These factors at large scales dominate the small-scale physics that is usually of more interest to the star-forming community, such as star formation (Federrath et al, 2010; Li et al, 2015), ion-neutral damping (Li et al, 2010; Xu et al, 2015), and outflow and stellar feedback (Stephens et al, 2018). The diffuse nature of the ISM allows one to model the dynamics of gas and phases with simple physical models that contain essential information like turbulence with magnetic fields (Yuen and Lazarian, 2020a,b; McClure-Griffiths et al, 2023).

The physics of interstellar filaments is highly connected to the properties of the "unstable neutral media" (UNM), which was previously considered an intermediate phase in the multiphase interstellar media (McKee and Ostriker, 1977). One of the most prominent features of filaments is their very high aspect ratio, frequently reported in observations. In Tab. 2, we have listed several examples in both diffuse HI and dense molecular clouds. It is evident that the long aspect ratio of filaments makes them unique quantifiers in observations.

It is well-known that certain types of turbulence exhibit universal relations in some statistical quantities. One of the most renowned is the Kolmogorov scaling (Kolmogorov, 1941), which states that, for 3D isothermal/adiabatic, incompressible, hydrodynamic turbulence, the power spectrum follows a simple scaling law:

$$E(k) \propto k^{-5/3} \quad (1)$$

Observationally, this scaling relation has been demonstrated from time to time. One of the most recent efforts is shown in Fig. 5, where a very large power

law is observed across almost six decades of length scales in the sky. Recently, Liu et al (2023) found results that seem to differ from that of Fig. 5. However, Liu et al (2023) focuses on regions that are gravitationally bound, and star-forming activities may impact the local turbulence energy spectrum. In fact, earlier studies (Li, 2018) have shown that the presence of strong gravitational collapse (Li et al, 2015) will cause the turbulence spectrum to deviate from the standard Kolmogorov cascade. The results presented in (Li, 2018) show that a universal spectral index is found across ISM from WNM to CNM.

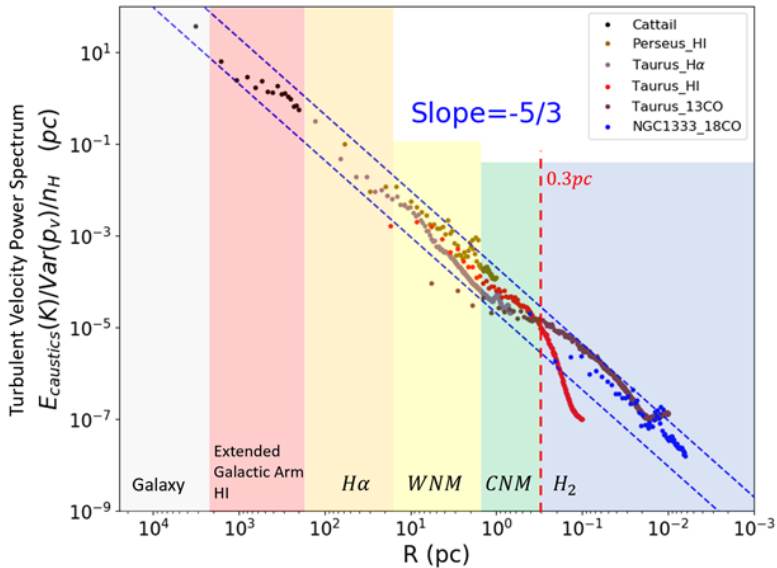


Fig. 5 The Big Power Kolmogorov Law for ISM velocity fluctuations spans from 10^4 pc to 10^{-2} pc, as analyzed via Yuen et al (2021) using archival data of ISM observations (see Yuen et al (2022) for detailed information). The universal cascade is evident, extending from turbulent velocities at the galactic arm scale down to star-forming hubs. To assist readers in recognizing the cascade, we have labelled the dominant scale for each phase and included auxiliary lines representing the Kolmogorov spectrum (the blue dashed lines). This information is derived from Yuen et al (2022).

Astrophysical turbulence is inherently magnetized and compressible, a topic that has been thoroughly investigated by numerous authors in the community (e.g., Cho and Lazarian 2003; Kowal et al 2007). The presence of compressibility in turbulence adds complexity to our understanding of how the three fundamental MHD modes (Alfven, slow, and fast modes), each characterized by different spectra and anisotropies, behave in various astrophysical phenomena. For instance, it is widely believed that the Alfven and slow modes play a central role in aligning the cold neutral media with the magnetic field (Lazarian and Yuen, 2018b) and controlling the transport of heat and particles across magnetic fields (Narayan and Medvedev, 2001; Maiti et al, 2021).

In contrast, fast modes are pivotal in the scattering and acceleration of cosmic rays ((Yan and Lazarian, 2002, 2004; Cho and Lazarian, 2005; Brunetti and Lazarian, 2007)). The composition of these modes strongly depends on the driving parameters (Makwana and Yan, 2020).

The magnetic component in multiphase turbulence provides additional directional guidance to the dynamics of ISM gases before reaching the H1-H2 conversion threshold (Beuther et al, 2016; Bialy et al, 2017). The morphology of ISM gases tends to be anisotropic along the local direction of the magnetic field, primarily due to the Goldreich-Sridhar cascade (Goldreich and Sridhar, 1995).

The fundamental idea behind Goldreich-Sridhar turbulence is as follows: When turbulence is strong ², it is postulated that the nonlinear time is of the same order of magnitude as the linear propagation time (Goldreich and Sridhar, 1995). In this scenario, the parallel and perpendicular length scales in the local frame of reference (Cho and Vishniac, 2000) exhibit the following scale-dependent relationship:

$$l_{\parallel} \propto l_{\perp}^{2/3} \quad (2)$$

A significant consequence of the Goldreich-Sridhar cascade is that, in cases where no additional heating and cooling processes are at play (Zweibel and Josafatsson 1983), observables in interstellar media driven by MHD turbulence tend to exhibit a filamentary nature. This phenomenon was well observed in early simulations (Cho and Lazarian, 2002; Federrath et al, 2010) and is also evident in observations (Heyer et al, 2008). As a result of this fundamental characteristic, it is widely believed that observational maps, whether linear (such as Column Density and Velocity Centroid, Esquivel and Lazarian 2005) or nonlinear (like Velocity Channel Maps, also known as PPV slices, Lazarian and Pogosyan 2000), are inherently filamentary due to the filamentary nature of their 3D counterparts. Here are some of the more common observables:

$$\begin{aligned} \text{Velocity Centroid:} \quad C(\mathbf{X}) &\propto \frac{\int_{\mathcal{L}} dz v(\mathbf{X}, z) \rho(\mathbf{X}, z)}{\int_{\mathcal{L}} dz \rho(\mathbf{X}, z)} \\ \text{Column Density:} \quad I(\mathbf{X}) &\propto \int_{\mathcal{L}} dz \rho(\mathbf{X}, z) \\ \text{Velocity Channel:} \quad p(\mathbf{X}, v_0) &\propto \int_{v \in v_0 \pm \Delta v/2} dz \rho(\mathbf{X}, z) \phi(v) \end{aligned} \quad (3)$$

Here, $\phi(v)$ is the kinetic kernel that incorporates contributions from turbulence, shear, and thermal broadening (Yuen et al, 2021). The prevalence of magnetized turbulence in the diffuse ISM allows the methods listed above to function both as identification techniques and as magnetic probes. We will delve into more technical aspects of how filamentary features in 3D multiphase

²In this review, we do not delve deeply into the fundamental properties of magnetized turbulence. The classification of "weak" and "strong" turbulence is based on the relative amplitude of the linear and nonlinear frequencies (see, e.g., Lazarian 2006; Schekochihin 2022), assuming that non-local transport is small.

interstellar media are translated into 2D representations in later sections. Due to observational limitations, 2D observational maps (as described in Eq. 3) that appear filamentary are not always indicative of 3D filaments, despite the strong correlation observed in both observations (Beuther et al, 2015) and simulations (Chen and Ostriker, 2015). For example, strong shocks are readily visible in compressible magnetized turbulence, and when viewed from the side, they can appear filamentary. Various projection effects have been well-documented; you can refer to Beaumont et al (2013) for more information. Moreover, when a 3D filament is projected using nontrivial observables like velocity channels, additional effects due to the velocity mapping (Lazarian and Pogosyan, 2000; Burkhart et al, 2013a; Beaumont et al, 2013; Yuen et al, 2021) come into play.

This additional effect can fragment real 3D density filaments that possess a line-of-sight velocity dispersion (typically nonzero for molecular clouds (Larson, 1981)) into pieces distributed across different channel maps. It can also combine two spatially separate 3D filaments with similar velocities into a single artificial filament in one channel map. We will discuss this nontrivial effect and its implications for several relevant observational findings in later sections.

It is crucial to emphasize that in the context of the diffuse ISM, filaments do not necessarily exhibit high density or intensity. In cases where gravity does not significantly concentrate high-density features, and when the plasma parameters are generally subsonic and sub-Alfvénic in the warm phase, the direct effect of the anisotropic MHD cascade primarily influences velocity (Lazarian, 2006).

Density fluctuations are influenced by velocity fluctuations and can be viewed as a mirrored response to the anisotropic velocity fluctuations, both for regions of high and low density (Kowal et al, 2007). However, as we mentioned in previous sections, MHD turbulence alone cannot fully explain the statistical features of ISM filaments observed in the sky (Kalberla et al, 2021; Ho et al, 2023). We will delve into this further in Section 3. In fact, the properties of HI filaments are closely connected to the underlying phases of the surrounding region.

Observational studies have attempted to measure the statistics between the three phases by comparing 21 cm line absorption and emission profiles. Heiles (2001) discovered that approximately 50% of the multiphase gas falls within a temperature range of 500 to 5000 K, indicating the presence of significant amounts of thermally unstable phases later referred to as Unstable Neutral Media (UNM) within the observed ISM. More recent absorption line studies by Murray et al (2018) suggest that 40% of the gases are in the UNM. Specifically, at least 20% of the total HI mass falls within the temperature range of 250 K to 1000 K, corresponding to the lower end of the UNM. It's worth noting that absorption line studies are limited to detecting the lower temperature end of the HI.

As evident from Murray et al (2018), a significant portion of UNM falls into the self-absorption regime. Consequently, previous observational studies that primarily focused on the structures of HI (e.g., Clark et al 2015; Clark

and Hensley 2019) likely underestimated the mass fraction of UNM and CNM (Seifried et al, 2022). Nonetheless, the above observations underscore the significance of UNM in the multiphase ISM, which shapes the morphology and statistical characteristics of filamentary features within it.

While we won't delve into the majority of the observed properties of molecular cloud filaments here, it's important to note that these filaments inherit their properties from their diffuse HI counterparts and still adhere to the same turbulence cascade (Larson, 1981; Yuen et al, 2022) until they reach scales that are small enough to enter the gravitational instability regime, which typically flattens the spectrum (Li, 2018), or until they are influenced by "micro-physics." The intricate interplay between turbulence, gravity, magnetic fields, and micro-physical processes has given rise to extensive research linking star formation (Li et al, 2017; Lazarian and Hoang, 2019) to the turbulence properties of molecular clouds (Mocz and Burkhardt, 2018).

Surprisingly, molecular cloud filaments exhibit a wider range of aspect ratios than their diffuse counterparts. The lower half of Tab.2 displays recent observations of filament aspect ratios. We caution readers that some of the "filaments" identified by observers are actually visually distinct and dynamically separated features that happen to result from the fragmentation of a single cloud. Therefore, the numbers reported in the literature should be interpreted with some caution. Fortunately, being isothermal and subject to strong turbulence allows for the quantification of aspect ratios based on simple plasma parameters, which we will discuss in Section 3.1. Notably, a study by Xu et al (2019) attempts to use the Goldreich-Sridhar scaling to explain the morphology of isothermal filaments. It is relatively straightforward to assess whether the numbers in Tab.2 are consistent with the Goldreich-Sridhar estimate by approximating the Alfvénic Mach number. In general, filaments in molecular clouds have following characteristics, but it is not the goal of this review to have an in-depth discussion (see, e.g., André et al 2014; Fissel et al 2016 and references therein, or Table 1):

1. Typically, filaments are denser, confined by self-gravity, and isothermal features (André et al, 2014).
2. Filaments can undergo fragmentation due to various factors, such as Jeans instability or other physical processes that disrupt their stability (Gómez and Vázquez-Semadeni, 2014; Vázquez-Semadeni et al, 2019).
3. The width of filaments range between ~ 0.03 pc to approximately ~ 0.15 pc (Fissel et al, 2016). However, it is still a debatable question whether there is an universal filament width across different scales and environments.
4. A "Plummer-like" density profile $\rho \propto (1 + r^2)^{-1}$ is often observed (Arzoumanian et al, 2019).
5. Various processes can create filamentary-like features, including outflows, stellar feedback, shocks from bubbles, or other micro-turbulence (e.g. Pineda et al 2023; Hacar et al 2023).

2.3 Filamentary structures seen in other context

While the term "filaments" is primarily used in the context of the diffuse interstellar medium and the star-forming community, the same concept has been extended to other types of measurements. Filamentary-like features have been observed in early measurements of synchrotron intensity and polarization maps (Gaensler et al, 2011) and even in cosmological research and intra-cluster medium (ICM). Here, we briefly review the literature that discusses filaments with scales smaller than the typical turbulence injection scale (Chepurnov and Lazarian, 2010). Filaments originating on larger scales typically arise from other physical processes, such as anisotropic thermal conduction in the case of the ICM (Chitsazzadeh et al, 2012). Some examples include (Kunz et al, 2012; Li et al, 2020).

Earlier observations of nonthermal emissions (e.g., Yusef-Zadeh et al 1984) revealed extensive filament-like features associated with poloidal magnetic flux tubes extending from the Galactic center. More recently, Gaensler et al (2011) observed a significant network of filaments in synchrotron polarization maps, which were later identified in numerical simulations as indicators of the sonic Mach number (Burkhart et al, 2013b) and as probes of the magnetic field (Lazarian et al, 2017; Lazarian and Yuen, 2018a). In fact, when analyzing observational maps of the diffuse interstellar medium using gradient-based algorithms, it is quite common to observe a network of filament-like features. These features can be easily reproduced by even the simplest high-resolution magnetohydrodynamic simulations, regardless of the Mach number (Yuen and Lazarian, 2020a). However, other mechanisms can create filamentary features in synchrotron polarization maps that are larger than the turbulence correlation length or even the injection scale typical of the interstellar medium (Chepurnov and Lazarian, 2010). For instance, the "North Polar Spur" is believed to have formed due to the influence of a local bubble (West et al, 2021).

There are other notable methods for detecting filaments, including dust emission and Faraday rotation maps. Dust polarization arises from the emission of non-spherical grains that align with their long axes perpendicular to the ambient magnetic field (see Andersson et al 2015). Similarly, polarization of starlight results from the differential extinction of aligned grains. Dust alignment is generally believed to occur due to radiative torques (RATs) (see Dolginov and Mytrophanov 1976; Draine and Weingartner 1996). The theory of RAT alignment is based on the analytical model presented in Lazarian and Hoang (2007) and further studies, such as Hoang and Lazarian (2008, 2016). Dust emission maps in the diffuse to moderately dense parts of molecular clouds are roughly linearly proportional to the actual gas density and can be treated as an alternative density tracer in observations.

Faraday rotation maps share very similar characteristics to synchrotron emission maps. In general, synchrotron emission depends on the distribution of relativistic electrons:

$$N_e(\mathcal{E})d\mathcal{E} \sim \mathcal{E}^\alpha d\mathcal{E}, \quad (4)$$

with the intensity of the synchrotron emission given by:

$$I_{\text{sync}}(\mathbf{X}) \propto \int dz B_{\perp}^{\gamma}(\mathbf{x}), \quad (5)$$

where $\mathbf{X} = (x, y)$ is the 2D position in the sky (POS) vector and $B_{\perp} = \sqrt{B_x^2 + B_y^2}$ represents the magnitude of the magnetic field perpendicular to the line of sight (LOS) along the z -direction. In general, $\gamma = (\alpha + 1)/2$ is a fractional power, and LP12 demonstrated that the statistics of $I(\alpha)$ are similar to those of $I(\alpha = 3)$. Therefore, it suffices to discuss the statistical properties in the case of $\alpha = 3$.

According to Lazarian and Pogosyan (2012), the synchrotron complex polarization function with Faraday rotation can be expressed as follows:

$$P_{\text{synch}}(\mathbf{R}) = \int dz \epsilon_{\text{synch}} \rho_{\text{rel}} B^2 e^{2i(\theta(\mathbf{R}, z) + C\lambda^2 \Phi(R, z))} \quad (6)$$

Here, ϵ_{synch} represents the emissivity of synchrotron radiation, and $\Phi(R, z)$ is the Faraday Rotation Measure (RM):

$$\Phi(R, z) = \int_{\infty}^z dz' \frac{1}{\sqrt{4\pi}} \rho_{\text{thermal}}(\mathbf{R}, z) B_z(\mathbf{R}, z) \text{ rad m}^{-2} \quad (7)$$

In this equation, ρ_{rel} is the relativistic electron density, ρ_{thermal} is the thermal electron density, and B_z is the magnetic field component along the line of sight (LOS). The C-factor is approximately 0.81 (Lazarian et al, 2017).

For frequencies lower than around 1 GHz, the Faraday Rotation Measure can exceed 2π , which results in a phase shift that causes a complete loss of information from the source. This leads to the concept of Faraday screening, which determines the maximum line-of-sight distance that can be observed in synchrotron emissions in the presence of a line-of-sight magnetic field. In the case of sub-Alfvénic turbulence, the source term $P_i = \rho_{\text{rel}} \exp(2i\theta(\mathbf{R}, z))$ is dominated by the mean magnetic field rather than the fluctuating field.

Two regimes, strong and weak Faraday Rotation, depend on whether the ratio of the scale sampled by polarization to the size of the emitting region, denoted as L_{eff}/L , is smaller (strong) or larger (weak) than unity:

$$\frac{L_{\text{eff}}}{L} \sim \frac{1}{\lambda^2 L} \frac{1}{\phi} \quad (8)$$

In this equation, ϕ is defined as $\max(\sqrt{2}\sigma_{\phi}, \bar{\Phi})$, where σ_{ϕ} represents the dispersion of the random magnetic field and $\bar{\Phi}$ is the average Faraday Rotation Measure. Given that the Faraday screen is typically non-zero in modern observations (e.g., LoFar), interpreting filamentary features in low-frequency maps requires exceptional care.

3 Theory of the formation of filamentary features in multi-phase interstellar media

In Section 1, we listed two fundamental questions related to cold neutral media filaments. From the above, we know how filaments are measured. However, it is still not clear why filaments in the ISM have different properties than those in simulations, nor the nature of these filaments. To understand why and how filaments are formed under the complex interplay of multiphase, multi-physics phenomena, we will need to delve into the theories and find insights into the effects of macro- (i.e., universal processes that affect all scales, e.g., turbulence, multiphase heating and cooling, etc.) and micro-physics (e.g., gravity on small scales, chemical evolution, HI shielding, etc.). These different physical processes act together to form the observed multiphase interstellar media. Understanding how physics controls the gas and phases is, therefore, the first step in answering the questions from Section 1.

The main goal of this review is to discuss the nature and appearance of filaments seen in the interstellar medium. Dense filaments in molecular clouds where the natural width (~ 0.1 pc, [André et al 2014](#); [Fissel et al 2016](#)), orientation (preferentially perpendicular to the B-field when density is high, ([Soler et al, 2013](#); [Li et al, 2013](#); [Xu et al, 2019](#))), and network-like structure has been well studied. However, their diffuse ISM counterpart is much less well understood.

Various models have been proposed to describe the formation of the diffuse filament:

1. Turbulence, which due to compression ([Padoan et al, 2007](#); [Federrath et al, 2010](#)), stretching, and mixing in the presence of a magnetic field ([Cho and Lazarian, 2003](#); [Kowal et al, 2007](#)) naturally produce filamentary features.
2. Other non-MHD physical mechanisms, e.g., heating and cooling ([Hennebelle, 2013](#); [Kritsuk et al, 2017](#); [Ho et al, 2023](#)), "turbulent conduction and mixing" ([Cho and Lazarian, 2004](#)), chemical evolution ([Gong et al, 2023](#)), and cosmic ray support ([Commerçon et al, 2019](#)), which can significantly reshape the filamentary features, particularly due to the ubiquity of unstable neutral media (UNM, [Murray et al 2018](#)).
3. Gravity, which plays a small role in confining the geometry of filaments ([Villagran and Gazol, 2018](#)).

As a result of these filaments formation mechanism from different ISM phases can exhibit very different visual properties, which we will discuss in **S_{3.1}** and **S_{3.2}** separately

The study of multiphase interstellar filaments was highly limited to small-scale simulations and hand-waving arguments until very recently when it became numerically feasible to perform large-scale simulations that could realistically model phase transitions and resolve complex physics. Unlike isothermal simulations, the use of direct numerical simulations (DNS) on multiphase media only began in the last two decades. The thermal instability relation

to turbulence and the analytic expression of the realistic cooling function have only been explored recently through the efforts of small-scale simulations (Koyama and Inutsuka, 2002; Kritsuk and Norman, 2002; Koyama and Inutsuka, 2004). The modern understanding of multiphase media thermodynamics includes a density-independent heating term and a temperature-dependent cooling term due to the Ly- α and CII lines, respectively. With the introduction of turbulence and a realistic cooling function, numerical studies have observed that a fraction of intermediate unstable neutral media (UNM) could exist stably throughout the evolution of hydrodynamical simulations (Kritsuk and Norman, 2002; Kim et al, 2014). This finding is further supported by subsequent MHD simulations with higher resolutions (Kritsuk et al, 2017). This UNM could significantly influence the dynamics of diffuse interstellar filaments (Ho et al, 2023), which are already influenced by the ubiquitous magnetized turbulence (Goldreich and Sridhar, 1995). In this chapter, we explore why filaments can maintain a large aspect ratio, supported by numerical evidence from the community, and why perpendicular filaments in the ISM are not seen in observations.

3.1 Goldreich-Sridhar Turbulence

GS95 scaling is one of the most important scalings in modern MHD turbulence theory. It was originally developed to explain why it is not possible to have a three-wave interaction in a turbulent cascade. The classical paper by Goldreich and Sridhar (1995) later became the foundation for the numerical exploration of compressible MHD turbulence.

It is important to note that the GS95 theory was originally developed for incompressible turbulence with an Alfvénic Mach number $M_A (= V_{inj}/V_A) = 1$. In the case of sub-Alfvénic turbulence ($M_A < 1$), there is an range of length scales where strong turbulence is not yet in play, meaning that the nonlinear time is still longer than the linear time. The turbulence in the range from the injection scale L_{inj} to the transition scale

$$l_{trans} = L_{inj} M_A^2 \quad (9)$$

is termed weak Alfvénic turbulence³. This type of turbulence keeps the l_{\parallel} scale constant while the velocities change as $v_{\perp} \approx V_L (l_{\perp}/L_{inj})^{1/2}$ (Lazarian and Vishniac, 1999). The cascading results in a change in the perpendicular scale of eddies, l_{\perp} , only. With the decrease of l_{\perp} , the turbulent velocities, v_{\perp} , decrease. Nevertheless, the strength of non-linear interactions of Alfvénic wave packets increases (see Lazarian 2016). Eventually, at the scale l_{trans} , the turbulence transitions into the strong regime, which obeys the critical balance condition proposed by GS95.

³It is worth emphasizing that, including Eq.16, the transition scale assumes that the largest energy is at the injection scale. In reality, every Fourier mode has its own transition scale, but since the injection scale has the most energy, numerical simulations might appear to have a transition regime at Eq.9 or 16. However, the actual transition should be a range of scales.

The situations where l_{trans} is less than the turbulence dissipation scale l_{diss} would require an unrealistically small Alfvénic Mach number M_A for typical ISM conditions. Therefore, in most cases, ISM turbulence transitions to the strong regime. If the telescope resolution is sufficient to resolve scales less than l_{trans} , we should observe the signature of strong turbulence in observations. For injection of roughly 100 pc (Chepurnov and Lazarian, 2009) and an Alfvénic Mach number of ~ 0.5 (Kalberla and Haud, 2015b), the corresponding length scale is $\sim 25pc$. Readers, however, should be reminded that the actual Mach number in ISM changes significantly due to phase transitions, and therefore the transition is believed to be a broadband of length scales.

The exact scaling was developed and studied extensively later by Lazarian and Vishniac (1999, see also Cho and Vishniac 2000; Maron and Goldreich 2001), among others:

$$\begin{aligned} \text{Critical Balance} : v_{\perp}/l_{\perp} &= v_A/l_{\parallel} \\ \text{Constant Energy Cascade } \perp B : \frac{v_{\perp}^3}{l_{\perp}} &= \text{const} \end{aligned} \quad (10)$$

Here, $v_{\parallel,\perp}$ denotes the velocity fluctuations parallel and perpendicular to the magnetic field, while $l_{\parallel,\perp}$ denotes the length scales parallel and perpendicular to the magnetic field. The first equation postulates the equivalence of nonlinear and linear timescales (See, e.g. Mallet et al 2015; Schekochihin 2022; Yuen et al 2023b for more recent discussions and experiments), while the second condition arises because MHD turbulence appears hydrodynamic when we consider only perpendicular directional motion⁴. By combining these two conditions, we can derive the length scales discussed earlier:

$$l_{\parallel} = L_{inj}^{1/3} M_A^{-4/3} l_{\perp}^{2/3} \quad (11)$$

For velocity v_l we use the critical balance relation ($\omega_{nl} \sim v_{\perp}/l_{\perp} \sim \omega_A = v_A/l_{\parallel}$):

$$\begin{aligned} v_l &= v_A \frac{l_{\perp}}{l_{\parallel}} \\ &= v_A M_A^{4/3} \left(\frac{l_{\perp}}{L_{inj}} \right)^{1/3} \\ &= v_{inj} M_A^{1/3} \left(\frac{l_{\perp}}{L_{inj}} \right)^{1/3} \end{aligned} \quad (12)$$

(see Xu et al 2015).⁵ These scalings are crucial for interpreting MHD turbulence in observations since GS95 scaling suggests a natural anisotropy parallel

⁴This is only possible when we consider that flux tubes are mobile under some sort of mechanism, e.g., Lazarian and Vishniac (1999) enables the reconnection diffusion mechanism to be in play

⁵Readers should be cautious in their choice of symbols. By "amplitudes," we actually mean the dispersion of velocity in real space since the Goldreich-Sridhar type argument was performed in Fourier space, and the inverse Fourier transform of squared Fourier amplitudes yields correlation functions.

to the direction of the magnetic field. Readers should be careful to note that the filaments referred to here are velocity or magnetic field fluctuations in incompressible turbulence, as density remains approximately constant over the course of dynamics. Treating density as an exact constant definitely does not apply to the multiphase media. In the next section we discuss how these scaling relations are modified in compressible turbulence.

The velocity and magnetic field striations created by strong Alfvénic turbulence provide guidance on how the morphology in 3D or 2D maps is correlated with the intrinsic statistics of MHD turbulence. Suppose we make an observation of "high velocity intensity" in a 3D cube by a simple intensity threshold at v_0 . Then, combining Eqs. 11 and 12, we can derive an expectation for the anisotropy of filaments defined by this threshold:

$$\text{Aspect ratio} = \frac{l_{\parallel}}{l_{\perp}}(v_l = v_0) = \frac{v_{inj}}{v_0 M_A} = M_A^{-4/3} \left(\frac{L_{inj}}{l_{\perp}} \right)^{1/3} \quad (13)$$

On the other hand, if one defines filaments via edge detection (e.g., Unsharp Mask, Rolling Hough Transform) with a definite Δx , then the aspect ratio is actually the derivative of Eq. 13 with respect to l_{\perp} with a correction factor that depends on the ratio $l_{\perp}/\Delta x$, as the edges of filaments are considered as two filaments in edge detection algorithms (Yuen et al, 2019). The correction factor arises from the fact that a thick filament can be misclassified as two very thin filaments. While the length of the filament is not altered via Eq. 11, the width is defined by the user-dependent choice Δx . In this case, one is not measuring the aspect ratio of the filament but rather a mixture of aspect ratios of thin filaments and the edges of thick filaments. Statistically, this increases the aspect ratio of the processed maps (Yuen et al, 2019). We can quantitatively describe the situation as follows:

$$\text{Aspect ratio} = \frac{1}{3} M_A^{-4/3} \left(\frac{L_{inj}}{l_{\perp}} \right)^{4/3} \times \begin{cases} 1 & (2\Delta x > l_{\perp}) \\ l_{\perp}/2\Delta x & (l_{\perp} > 2\Delta x) \end{cases} \quad (14)$$

In other words, the "aspect ratio" of filaments, even in the simplest case, has obvious dependencies on how it is defined.

The projection of filaments into 2D space is much more complex. In Section 3.3 we discuss the channel map effect, which was first systematically studied by Lazarian and Pogosyan (2000). However, here we first discuss the global-to-local frame transformation effect, first proposed by Cho and Vishniac (2000) (See also Chandran 2000; Cho and Lazarian 2003; Yuen et al 2023c,b). All the formulae above describe a filament in the local frame of reference. However, when filaments are projected onto a 2D plane, the frame effect has to be taken into account. In the following, we use the same mindset as Yuen et al (2023c) in discussing how the filaments are projected onto the 2D plane, assuming we are computing the unnormalized velocity centroid ($C \sim \int dz v(x, y, z)$). For simplicity, we will also assume the mean magnetic field is perpendicular to the

line of sight. We have to remind the reader that the anisotropy of the projection of a particular component of MHD variable depends on contributions from both the scaling relation (Eq. 11) and the "tensor anisotropy" (Yuen et al, 2023c). For the tensor anisotropy, it is out of scope of the current review.

In the global frame of reference, the scale-dependent anisotropy is lost (see, e.g., Cho and Vishniac 2000; Kowal et al 2007). This is because for filaments with dimensions $L \times H$ where $L \gg H$, its magnetic field wanders relative to the mean field with an angle dispersion of $\delta\theta \propto M_A$ (Yuen et al, 2023c). The global frame anisotropy is therefore determined by the most probable length and width measured with respect to the global magnetic field direction, which is independent of the filament dimension in the local frame of reference. The most probable length for a statistically sufficient collection of wandering filaments is L , while the probable width is $L \sin\theta$, in small angle:

$$\text{Aspect ratio} \propto M_A^{-1} \quad (15)$$

which allows one to observe a different dependence on M_A compared to Eq. 14. However, the length of the observed filament is still relevant to the intrinsic turbulent properties given by Eq. 11. To measure the true dimensions of filaments, one requires the collection of filaments along the line of sight to be statistically sufficient, and as a result, individual imprints of 3D filaments can be separable via vision identification algorithms, and we revert to Eq. 13 or Eq. 14 depending on the type of algorithms one uses

Readers should be reminded that we are discussing velocity or magnetic field striations in the incompressible limits. Fluctuations of velocity and magnetic fields are symmetric about the mean value as long as there are no other physical processes favoring the collection of either high or low intensity values. As a result, the anisotropy of low-intensity pixels induced by velocity or magnetic field fluctuations also carries statistical meaning in the GS95 framework, which is exactly the case for velocity channel or synchrotron polarization maps.

It should also be noted that the presence of strong turbulence allows magnetic reconnection via stochastic diffusion to happen (Lazarian and Vishniac, 1999). A recent proposal Kumar et al (2020) suggests that the formation of Tiny Scale Atomic Structure (TSAS, Heiles and Troland 2003) could originate from reconnection. Some evidence for this is reported in numerical simulations (Fielding et al, 2023), even though there they refer to plasmoid instability in terms of the reconnection mechanism. We elect to discuss the possibility of reconnection-driven processes in a later publication and invite readers to read the review (Lazarian et al, 2020).

3.1.1 Compressible MHD turbulence

The first correction of the model above (c.f. Eqs. 13, 14, 15) for filaments in Table 2 is to include compressibility. Here we briefly summarize the scaling laws *in the local frame of reference* for compressible MHD turbulence as done in Lazarian and Yuen (2018b). If the energy is injected with the injection velocity

Table 3 Regimes and ranges of MHD turbulence. From Lazarian et al (2022b)

Type of MHD turbulence	Injection velocity	Range of scales	Motion type	Ways of study
Weak	$V_L < V_A$	$[L_{inj}, l_{trans}]$	wave-like	analytical
Strong sub-Alfvénic	$V_L < V_A$	$[l_{trans}, l_{diss}]$	eddy-like	numerical
Strong super-Alfvénic	$V_L > V_A$	$[l_A, l_{diss}]$	eddy-like	numerical

L_{inj} and l_{diss} are injection and dissipation scales, respectively

$M_A \equiv v_{inj}/v_A$, $l_{trans} = L_{inj}M_A^2$ for $M_A < 1$ and $l_A = L_{inj}M_A^{-3}$ for $M_A > 1$.

V_L that is less than the Alfvén speed V_A , the turbulence is *sub-Alfvénic*. In the opposite case, it is *super-Alfvénic*. Turbulence scaling for different regimes can be found in Table 3. We now briefly describe the regimes in Tab. 3 and how GS95 scalings are modified in compressible flows. A more extensive discussion can be found in the review by Brandenburg and Lazarian (2013).

In the case of compressible turbulence, the MHD modes can be separated into *to at least*⁶ three MHD modes: Alfvén, slow, and fast modes, where only the last two modes contribute to density fluctuations. These magnetosonic modes behave very differently than of Alfvén modes.

Let us first discuss slow modes. In the case of high plasma $\beta = 2M_A^2/M_s^2$ subsonic turbulence, density fluctuations are enslaved by their velocity counterpart (Lazarian, 2006), and thus the aspect ratio of density fluctuations can be modeled by the argument made for velocity striations in Eq. 11. The properties of low β slow modes are much more complicated; earlier studies suggested that the anisotropy imprint of low β slow mode is actually weaker than that of the Alfvénic counterpart (Cho and Lazarian, 2003; Kowal et al, 2007; Kowal and Lazarian, 2010). The most extensive recent analysis is Makwana and Yan (2020), where Fig. 9 suggests that the low β anisotropy is somewhere between GS95 and isotropic and systematically weaker than that of the Alfvénic mode. Nonetheless the anisotropy of slow modes is still believed to have a strong correlation to GS95 in small scales, and the same toolset that we discussed in Eq. 13 can be used for slow modes *as long as the anisotropy is scale-dependent*.

Fast modes are much more complicated and require extensive studies since they are highly related to the density structures formed in the interstellar media (See also statistical analysis from Makwana and Yan (2020), and recent satellite observations from Zhao et al (2023b,a)). In subsonic regimes, fast modes are isotropic and exhibit a $-3/2$ or -2 spectrum (Makwana and Yan, 2020). Fast mode in high β cases is the main contributor of density fluctuations, but it is usually not important unless the sonic Mach number is over unity. Shock-induced filaments can be arbitrarily compressed in the case of

⁶Different from most of the ISM literature, we emphasize the presence of zero temporal frequency entropy modes since the ISM temperature profile is not simple (See Fig. 2).

isothermal media from classical analysis, but can only be compressed by a factor of $(n + 1)/(n - 1)$ for adiabatic cases where n is the adiabatic index (See a comprehensive analysis from [Xu et al \(2019\)](#)⁷). We can see that the thermal properties of turbulent plasma, characterized by the adiabatic index n , are crucial in explaining the aspect ratio of shock-driven filaments. In the context of a multi-phase interstellar medium (ISM), the adiabatic index could be $n < 0$ for unstable natural media, due to the strong cooling effect. This scenario promotes a pressure gradient directed toward the dense center, thereby favoring the formation of shock-induced turbulence, even when the sonic Mach number M_s is only slightly greater than unity.

Fast mode in supersonic low β is the most complicated case of all kinds. Interstellar media is almost always low β when the length scale is above the ion-neutral decoupling scale (~ 0.1 pc), [Xu et al 2015](#)). However, not until the ISM enters the lower end of the unstable phase or the cold phase will the sonic Mach number become larger than 1. In the case of molecular clouds, the sonic Mach number can > 10 ([Padoan et al, 2006](#)). Very importantly, the high density features are typically perpendicular to the mean magnetic field, contrary to the common observations on the observed CNM emission lines ([Clark et al, 2015](#); [Kalberla et al, 2020](#)), suggesting that these shock-like features are unlikely the visible CNM in the HI emission lines but denser features in the interstellar media. A handy estimate of the aspect ratio of these features can be obtained by estimating how much compression can the dense features have in different thermal regimes: In the case of an adiabatic equation of state (diffuse part of CNM), $n = 5/3$, and therefore the maximum compression is $\rho_{new}/\rho_{original} \sim 4$. Assuming the gas was originally isotropic and being compressed by pressure, then the resultant aspect ratio is 4. For the denser part of CNM and diffuse H_2 , the compression is at maximum M_s , and as a result, the aspect ratio is also M_s .

3.1.2 Super-Alfvenic Turbulence?

While at first glance, super-Alfvenic turbulence does not appear to have any relation to magnetically aligned filaments, we have to remind the readers that the cold neutral media is believed to be mildly super-Alfvenic (See, e.g., [Kalberla and Haud 2018](#)), despite the fact that the ambient warm and unstable phases are in the sub-Alfvenic regime. We will go through the complexity of multiphase turbulence later in this section, but we would like to first outline some basic properties of super-Alfvenic turbulence.

In the case of isothermal MHD turbulence and if $V_L > V_A$, at large scales, magnetic back-reaction is not important, and up to the scale (see [Lazarian 2006](#)):

$$l_A = L_{inj} M_A^{-3}, \quad (16)$$

the turbulent cascade is essentially a hydrodynamic Kolmogorov cascade. At the scale l_A , the turbulence transfers to the trans-Alfvenic turbulence described

⁷We have to specifically note that when $M_s, M_A > 1$, there is a maximum compression ratio that depends on the Mach numbers.

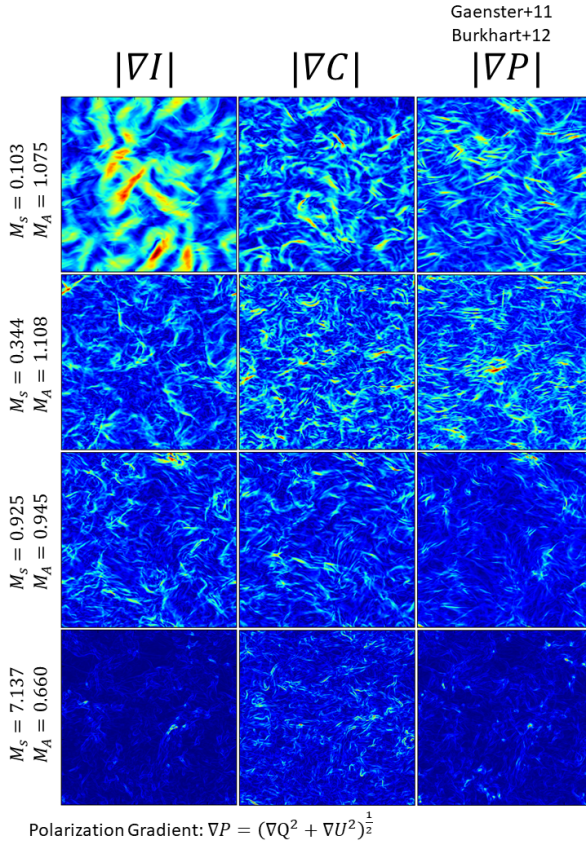


Fig. 6 A tabulation on how filamentary features visually look like for various M_s and M_A . The mean field is parallel to the horizontal axis. From [Yuen and Lazarian \(2020a\)](#).

by GS95 scalings, i.e., anisotropy of turbulent eddies starts to occur at scales smaller than l_A , in a form very similar to Eq.11 but without the $M_A^{-4/3}$ factor and replacing L_{inj} with l_A ([Xu et al, 2019](#)):

$$l_{\parallel} = l_A^{1/3} l_{\perp}^{2/3} = L_{inj}^{1/3} M_A^{-1} l_{\perp}^{2/3} \quad (17)$$

In other words, small-scale features in super-Alfvénic turbulence are still anisotropic (See, e.g., [Kowal and Lazarian 2010](#)), but the deviation of the Alfvénic Mach number from unity *suppresses* the anisotropy of filaments. A similar discussion on how frame transformation applies to Eq.17 (c.f. Eq.15) can be performed, but since $M_A > 1$, filaments will appear to be randomly

Mode	Power spectra $E(k)$	Anisotropy factor	Frame vector
Alfven	$k^{-5/3}$	$\exp(-M_A^{-4/3} k_{\parallel}/k_{\perp}^{2/3})$	ζ_A
Slow (low β)	$k^{-5/3}$	varies ⁸	ζ_S
Slow (high β)	$k^{-5/3}$	$\exp(-M_A^{-4/3} k_{\parallel}/k_{\perp}^{2/3})$	ζ_S
Fast (low β)	$k^{-3/2}$	1	ζ_F
Fast (high β)	$k^{-3/2}$	k_{\perp}^2	ζ_F

Table 4 A summary of the theoretical expectations of the turbulence scaling laws for sub-Alfvenic and subsonic turbulence. Summarized from [Cho and Lazarian \(2003\)](#); [Makwana and Yan \(2020\)](#). From [Yuen et al \(2023c\)](#).

oriented around the mean magnetic field direction after projection along the line of sight.

3.2 Multi-phase Micro-physics: Thermal instability, Turbulence-fueled unstable phases, Turbulence Heat Transport

3.2.1 Brief introduction

Turbulence in the ISM is much more complicated. The ISM community usually divides the ISM study into two distinct categories: (1) the study of very diffuse, multiphase neutral HI turbulence, and (2) the study of ISM turbulence within molecular clouds that is typically supersonic, isothermal, trans- to sub-Alfvenic, and often sub-critical⁹. While early numerical works already explored the interaction of phase and turbulence ([Audit and Hennebelle, 2005](#); [Hennebelle and Audit, 2007](#); [Hennebelle et al, 2007](#)), it is only very recently (e.g., [Hennebelle 2013](#); [Kritsuk et al 2017](#); [Kim et al 2016, 2017](#); [Kim and Ostriker 2017, 2018](#); [Kim et al 2018](#); [Seifried et al 2020a,b](#); [Yuen et al 2021](#); [Ho et al 2023](#); [Fielding et al 2023](#)) that the community started studying how turbulence continuously cascades from the multiphase media to the dense molecular clouds.

The heating and cooling of ISM gases has been discussed multiple times in the literature (See, e.g., [Koyama and Inutsuka 2002](#); [Wolfire et al 2003](#); [Draine 2011](#); [Klessen and Glover 2016](#)). Here, we discuss the basics and the consequences of the phase diagram depicted in Fig. 8. Table. 5 lists the phases of ISM and their typical physical parameters, and in Fig. 6 we show how varying M_s and M_A changes the shape of filaments in simulations. The most important heating process in the diffuse ISM is photoelectric heating. There are also multiple cooling processes. Ly- α dominates the cooling of the diffuse hot ISM, while C^+ dominates the cooling of the denser parts. Typically, one could model the cooling (of C^+) and heating via the following construction

⁹This means the magnetic criticality, i.e., the ratio of gravitational energy to that of magnetic energy, is smaller than 1

Table 5 The typical M_s, M_A, β values for interstellar media and molecular clouds, $n_H, \delta v$ for molecular clouds from [Draine \(2011\)](#); [Kalberla and Haud \(2018\)](#); [Yuen et al \(2021\)](#); [Ho et al \(2023\)](#); [Yuen et al \(2023a\)](#), β is from [Ho et al \(2023\)](#).

Phases	$n_H(\text{cm}^{-3})$	$\delta v(\text{km/s})$	$\beta = 2M_A^2/M_S^2$	Typical temperature (K)
WNM	0.1 – 1	10 – 17	~ 100	5500 – 10000
UNM	1 – 10	6 – 10	~ 1	200 – 5500
CNM	10 – 50	3 – 5	~ 0.1	50 – 200
GMC Complex (H_2)	$> 10^2$	4 – 50	~ 0.01	< 50

([Zweibel and Josafatsson, 1983](#)):

$$\begin{aligned} \text{Heating rate : } \Gamma_{pe} &\propto n_{HI} \\ \text{Cooling rate due to } C^+ &:\Lambda \propto n_{HI}^2 \sqrt{T} \exp\left(-\frac{184}{T}\right) \end{aligned} \quad (18)$$

For the multiphase ISM, the typical equation of state (EOS) for HI is adiabatic for WNM and CNM: $P \propto \rho^{5/3}$. There is a particular range of densities (and temperatures) determined by the heating and cooling rates. Between the warm and the cold phase, there is a peculiar phase named **Unstable Neutral Media** (UNM), which exhibits unusual physical properties related to turbulence. In particular, $P_{UNM} \propto \rho^n$ with $n < 0$. The ubiquitous existence of UNM (about 20% in both mass and volume fraction, [Kalberla and Haud 2015b](#)) is crucial for the formation stability of the CNM as turbulence interacts with UNM in a non-trivial manner. Readers should note that in some of the literature, there are exact cut-offs for the WNM and CNM temperatures. This is theoretically incorrect as the phase transition is a function of the two rates. The formation of the intermediate UNM phase is highly dependent on various factors. For instance, [Wolfire et al \(2003\)](#) modeled the formation of UNM phases as a function of galactic distance. They found that at a distance of 18 kpc from the galactic center, the cooling rate is not sufficient for the formation of CNM. Turbulence in the WNM is subsonic and sub-Alfvénic, while for CNM it is supersonic ([Kalberla and Haud, 2019](#)). The turbulence conditions for the unstable phase are at the borderline and likely do not obey the critical balance condition (i.e., no GS95 scaling). Nevertheless turbulence cascades continuously over all three phases ([Yuen et al, 2022](#)).

In the case of molecular clouds, dust cooling and ambient HI-shielding play an important role in maintaining the isothermality of molecular clouds. Molecular clouds are typically modeled as isothermal, as temperature fluctuations are negligible (see Tab.5). Turbulence is typically highly supersonic ($M_s > 10$) and highly compressible ($\beta \ll 1$). It is also well-known that molecular clouds are highly magnetized, either inferred from Zeeman measurements ([Crutcher et al, 2010](#)) or the hourglass morphology observed in polarization ([Li and Henning, 2011](#)). It is typical to model the turbulence in molecular clouds as trans-Alfvénic or sub-Alfvénic and highly self-gravitating, in contrast with the multiphase where self gravity has a minimal effect, see [Villagran and Gazol 2018](#)).

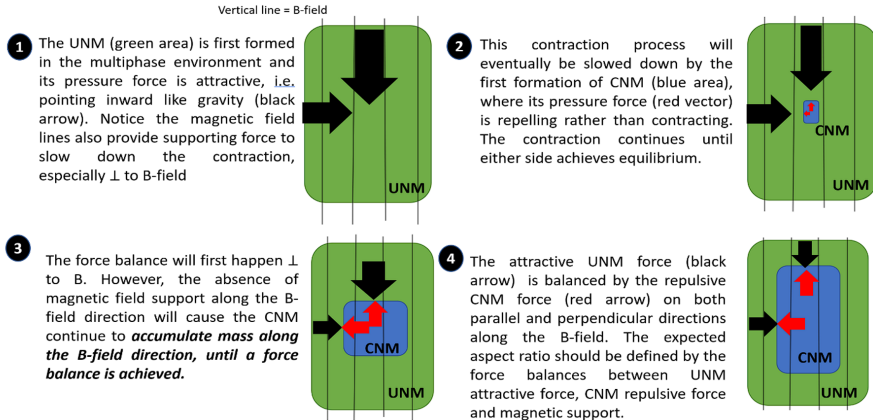


Fig. 7 An infographic describing the force balance model from [Ho et al \(2023\)](#) decides the length of CNM filament in magnetized multiphase system. Notice the aspect ratio of CNM predicted by this force balancing model is shorter than the GS95 estimate.

3.2.2 Thermal instability constrains cold filament anisotropy

The existence of multiphase heating and cooling definitely affects the dynamics and spatial properties of the CNM because the assumptions of Goldreich-Sridhar turbulence (which holds at large scales) do not apply as we cascade from large roughly 10 pc to small scales roughly 1 pc. While the velocity perturbation δv remains more or less constant ([Ho et al, 2023](#)), both the thermal and Alfvénic speeds undergo significant changes during phase transitions. Consequently, the cold phase has both its sonic and Alfvénic Mach numbers one order of magnitude higher than those of the warm phase, even though δv remains constant ([Kalberla and Haud, 2018](#)). In terms of the Goldreich-Sridhar critical balance postulate, this means that the phase speed of Alfvén waves suddenly drops by a factor of 10, resulting in evident changes in the corresponding anisotropy formed under the Goldreich-Sridhar turbulence framework. Indeed, as observed by [Ho et al \(2023\)](#), the actual measured filament aspect ratio from multiphase numerical simulations significantly deviates from the Goldreich-Sridhar estimate. This deviation appears to be consistent with earlier studies as well ([Hennebelle, 2013](#)).

How do multiphase simulations (e.g., [Hennebelle 2013](#); [Kritsuk et al 2017](#); [Kim and Ostriker 2018](#); [Ho et al 2023](#); [Fielding et al 2023](#)) differ from isothermal turbulence studies of ([Cho and Lazarian, 2003](#); [Kowal and Lazarian, 2010](#)) in terms of turbulent cascades? Considering the “onion” model of the ISM ([McKee and Ostriker, 2007](#)) and the prevalence and dominance of the UNM, ([Murray et al, 2018](#)) in terms of both mass and volume fractions, it is likely that it plays a significant role in shaping the CNM. [Ho et al \(2023\)](#) pointed out that the presence of massive unstable phases acts as a stabilizer for the formed cold phase, and prevents the growth of log filaments. This is because maintaining a negative adiabatic index over a substantial period creates local pockets with

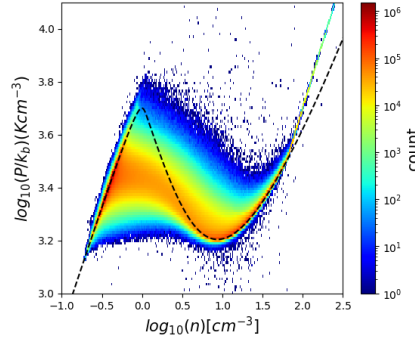


Fig. 8 A typical phase diagram for multiphase ISM simulations. From Ho et al (2023).

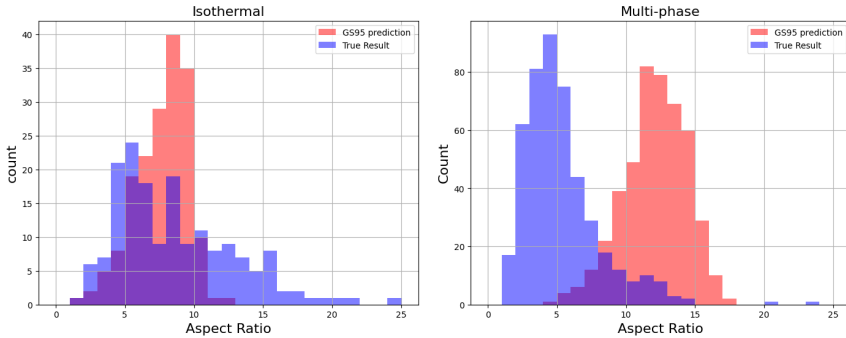


Fig. 9 Histogram of aspect ratio between true filament aspect ratio and GS95 prediction ($\frac{l_{\parallel}}{l_{\perp}} \sim M_A^{-4/3} (\frac{L_{inj}}{l_{\perp}})^{1/3}$). Left: isothermal case ($M_S \approx 6, M_A \approx 0.8, N^3 = 792^3$. Right: Multi-phase strong B-field case.) Adopted from Ho et al (2023).

inward-falling "gravity-like" pressure terms. These local pockets condense further and develop into cold clouds similar to the situation with Jeans instability. A graphic describing this process is given in Fig. 7. Any inward-falling collapsing forces are counterbalanced by turbulence and the magnetic field until the former becomes dominant, triggering instability. However, unlike gravity, the inward-falling force only acts within specific density and length scale roughly 1 pc ranges corresponding to the unstable phase.

Ho et al (2023) perform a quantitative analysis and recognize two regimes, depending on the relative pressure in the unstable and the cold phases (See Fig.10):

1. UNM compression regime

$$0 < \frac{2}{25.6} \left(\frac{n_{peak}}{n_c} - 1 \right) < \frac{l_{\perp}}{l_{U,\perp}}. \quad (19)$$

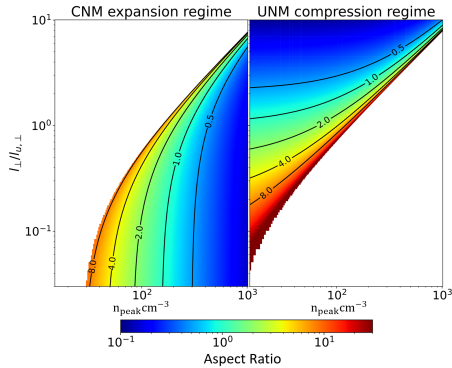


Fig. 10 The analytical prediction (Eq. 20) illustrates how the aspect ratio varies as functions of the peak hydrogen number densities of the cold and unstable phases (n_{peak}) and the ratio of the widths of CNM and UNM ($l_{\perp}/l_{U,\perp}$), using typical Mach numbers for CNM ($M_S \approx 5$) and $M_A \approx 0.8$. The iso-contours represent the values of the aspect ratio. When the aspect ratio is greater than 1, the filament is parallel to the magnetic field (B), while when it is less than 1, the filament is perpendicular to B . This analysis is adopted from [Ho et al \(2023\)](#).

2. CNM expansion regime

$$\frac{l_{\parallel}}{l_{\perp}} = \frac{M_S^2}{M_A} \left[2 \left(\frac{n_{\text{peak}}}{n_C} - 1 \right) - 25.6 \frac{l_{\perp}}{l_{U,\perp}} \right]^{-1}. \quad (20)$$

which is very different from the GS95 expectation (See Fig.9).

[Ho et al \(2023\)](#) observed that the filaments formed in the case of a multiphase turbulence system generally have a shorter aspect ratio than that predicted by GS95. Recall from the previous section that the maximum compression for adiabatic gases is 4. The unstable phase allows the condensation of the cold phase to reach a certain density threshold, but the aspect ratio of CNM formed in realistic multiphase numerical simulation remains less than that estimated using Goldreich-Sridhar. This is because the inward-falling pressure formed by phase dynamics is isotropic in nature. Long filaments (in the sense of greater than ~ 20) are dynamically unstable as long as the unstable phase is present for a sufficiently long period of time (See Figure 11).

3.2.3 Unstable phase fraction bumped up by turbulence

Earlier numerical studies (e.g., [Hennebelle 2013](#); [Kritsuk et al 2017](#); [Kim and Ostriker 2018](#)) and observational studies (e.g., [Murray et al 2018](#); [Kalberla et al 2020](#)) already show that the fraction of the unstable phase is significant. A natural question regarding the dynamics of the unstable phase, as discussed in the previous section, is whether the unstable phase should indeed be "unstable" and dissipate rather quickly with a short dynamical time, as proposed in [McKee and Ostriker 1977](#). An important question naturally arises: how does

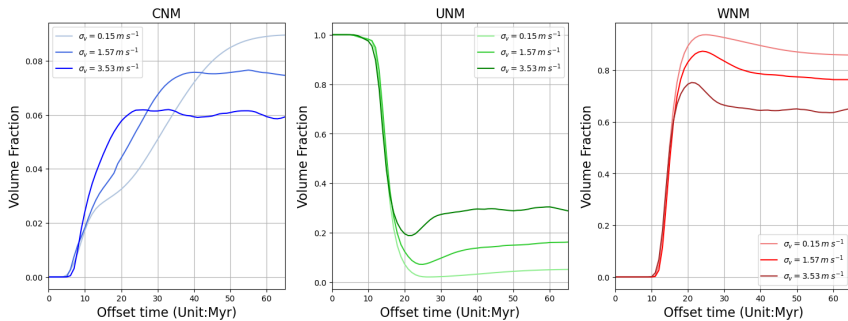


Fig. 11 The evolution of three phases in three multiphase simulations with different turbulence levels. It is rather clear that (i) the increase of turbulent velocity dispersion (denoted by σ_v) increase the fraction of unstable phases (ii) the three phases are in dynamical equilibrium for an extended period of time (~ 20 - 40 Myr depending on the phases). From Ho, Yuen, Lazarian (submitted).

the interstellar medium sustain such a large amount of what should be unstable phases?

Earlier literature (e.g., Gazol et al 2001; Kritsuk and Norman 2002; Wolfire et al 2003) already suggested that turbulent motions play a crucial role in determining the temporal and spatial structure of the phases. Of particular interest is the regime discussed in Wolfire et al 2003, where $\rho(P_{WNM,max}) < \rho < \rho(P_{CNM,min})$, leading to the natural appearance of two stable phases. Physically, when turbulence levels are strong enough, more cold phases are cycled back to the warmer phases. This phenomenon has been observed when turbulence levels are sufficiently high (Kritsuk et al, 2017). However, the exact mechanisms by which turbulence controls the three-phase structure remain a mystery.

Figure 11 illustrates how variations in turbulence energy injection affect the relative fraction of unstable phases. Clearly, as more turbulent energy is injected into the turbulence box, the fraction of the unstable phase increases. Moreover, the phases remain in a stable fraction for an extended period, and with higher turbulent energy injection, the cold phase enters a steady state more rapidly. This may appear counter-intuitive at first glance. However, when we consider the "stability" effect discussed in the previous section, it becomes evident that the increased fraction of the longer-lasting unstable phase actually contributes to the formation and maintenance of both the temporal and spatial stability of cold gases.

3.2.4 Heat transport from magnetized multiphase turbulence

In the previous two sub-subsections, we discussed the unexpectedly long lifetime of the unstable phase and how it prevents the formation of long filaments. However, the relationship between heat transfer and turbulence remains unresolved. Naively, turbulence acts as both a free energy source that pumps up

the cold phase and sustains the thermal phase in the unstable regime. The latter forces the cold phases to condense. In other words, turbulence acts as both a heat source and a stabilizer for the unstable-cold phase complex, creating some sort of equilibrium between them.

Turbulence can also diffuse energy in a similar fashion to thermal diffusion. In the case of the more diffuse intra-cluster medium (Narayan and Medvedev, 2001; Kunz et al, 2012; Li et al, 2020), the heat transfer due to thermal conduction and turbulent transport is of comparable magnitude (only differing by a factor of 5 compared to Spitzer's (Spitzer, 1962) value when the magnetic field is chaotic (Narayan and Medvedev, 2001)). Cho et al (2003) briefly discussed that in the case of magnetic field wandering and mixing (See Lazarian and Vishniac 1999; Kowal et al 2012) the heat transport by turbulence is about 100 times more effective than thermal conduction. However, Cho et al (2003) used fictional temperature values for the cold and warm phases that significantly deviate from modern observations (see Tab.5). Correcting for this fact would yield a ratio of "turbulent conductivity" to Spitzer's value (Spitzer, 1962) on the order of $\kappa_{turb}/\kappa_{Sp} \sim O(1000)$, suggesting that heat exchange is mainly performed by turbulence transport. In the cold phase, the existence of turbulence quickly equalizes the temperature within it.

Does anisotropic turbulence provide anisotropic temperature equalization within cold neutral media? Thermal instability from anisotropic conduction was proposed as early as Field (1965) and later extensively studied by Choi and Stone (2012), where the latter assumes an anisotropic heat conduction tensor. A characteristic length from Field (1965) suggests that heat can be equalized within one "Field's length":

$$\lambda_F = \frac{\text{Conduction-Diffusion}}{\text{Cooling}} \propto \left(\frac{\kappa T}{\rho^2 \Lambda} \right)^{1/2} \quad (21)$$

which determines the "coherent thermal length" of a cold filament. Choi and Stone (2012) construct an anisotropic thermal tensor and propose that the parallel conductivity $\kappa_{\parallel} \propto \langle B \rangle^2$, while that of the perpendicular conductivity $\kappa_{\perp} \propto \delta B^2$, which gives an aspect ratio scaling to Alfvénic Mach number ($\delta B / \langle B \rangle \sim M_A$):

$$\frac{\lambda_{F,\parallel}}{\lambda_{F,\perp}} \sim M_A^{-1} \quad (22)$$

which they test in numerical simulations of the intra-cluster medium. However, this construction via anisotropic thermal tensor has an immediate issue if we want to apply this argument to the ISM: Thermal transport in the ISM, as we argued earlier, is dominated by turbulence.

One obvious method of estimating the effect of turbulence thermal transport via the Field's length argument is to replace κ in Eq. 21 with κ_{dynamic} , which can be approximated using the characteristic length and velocity from

a given turbulence model:

$$\kappa_{\text{dynamic},\parallel/\perp} \rightarrow l_{\parallel/\perp} v_{\text{turb},\parallel/\perp} \quad (23)$$

This estimation yields a scaling of $\frac{\lambda_{F,\parallel}}{\lambda_{F,\perp}} \propto M_A^{-4/3}$, similar to the direct GS95 estimate performed in the previous subsection (Eq. 13). However, this direct substitution does not consider the effect of turbulence-thermal phase interaction that we discussed in the previous two sub-subsections.

So, how do we model the aspect ratio of cold neutral media with the knowledge from the previous subsections? Yuen et al. (submitted) performed a quantitative treatment of how turbulence interacts with radiative heating and CII cooling, changing the heat transport properties in the multiphase ISM. It was discovered that the adiabatic index, which controls Eqs. 19 and 20, is related to the plasma Mach numbers: $n \propto M_s^2/M_A^2$. From there, Yuen et al. (submitted) discussed that the anisotropy can be larger than the thermal instability estimate of the above equations by flattening n , while still staying smaller than the GS95 estimate (Eq. 13).

3.3 Observational Constraints: Projection, Mapping, Velocity caustics and absorption

Observational constraints can hinder the application of the above theories. How 3D turbulent information is mapped into 2D observational space was comprehensively developed by the framework of Lazarian and Pogosyan (2000) (see also Lazarian and Pogosyan 2004, 2006, 2008, 2012, 2016; Kandel et al 2016, 2017; Yuen et al 2021, 2023c). The essence of the LP statistical theory aims to answer a very simple question: For a given statistical model of turbulence in 3D, how do the statistics of observables behave? While this question may sound trivial, the difficulty increases dramatically when magnetic fields and turbulence are both in effect, not to mention the effects of radiative transfer (in particular, absorption). There are two types of transfer considered under the framework of LP statistical theory:

1. How is the observed column density or velocity-like observables correlated with the 3D statistics of turbulent density and velocity in emissions (Lazarian and Pogosyan, 2000; Kandel et al, 2016, 2017; Yuen et al, 2021; Yuen and Lazarian, 2020a,b; Lazarian et al, 2022b) and absorption maps (Lazarian and Pogosyan, 2004, 2006, 2008)?
2. How are the observed polarization fluctuations (e.g., Stokes Q, U, polarization angle, polarization percentage) correlated with the 3D fluctuations of polarization (Lazarian and Pogosyan 2012, 2016; Lazarian et al 2022b; Yuen et al 2023c; Lazarian et al 2022a; Malik et al 2023)?

These questions are exceptionally critical when discussing "filaments" observed via different instruments. A simple example is that for a given 3D filament oriented at a certain nontrivial angle with respect to the line of sight, the projection of it will appear as a shorter filament. A less trivial examples are

the filaments observed in the velocity channel space. When HI absorption is in play (Theory: Lazarian and Pogosyan 2004, 2006, 2008; Beuther et al 2016, Numerics: Seifried et al (2022), Observation: Murray et al 2018), a significant portion of the cold phases is actually optically thick. Are the filaments that we observe in HI emission maps cold or unstable phases? In this subsection, we will briefly go through the theories of statistical mapping (Lazarian and Pogosyan, 2000, 2004, 2006, 2008, 2012, 2016; Kandel et al, 2016, 2017; Yuen et al, 2021, 2023c), and then we will discuss how they impact our statistical measurements of filaments when using different methods outlined in Section 2.

3.3.1 Statistical Mapping: Intensity and Centroid Map

The construction of the statistical theory for observables usually involves correlation and structure functions using a suitable frame. Since MHD turbulence exhibits anisotropy along the mean magnetic field, the statistical properties of the 3D turbulence variables differ parallel and perpendicular to the mean magnetic field. Earlier literature (Batchelor, 1946; Chandrasekhar, 1950; Matthaeus and Smith, 1981; Oughton et al, 1997) has utilized this property to characterize turbulence anisotropy. We can represent the correlation function (and also the structure function) of a vector turbulence variable $X_{i=x,y,z}$ in the axis-symmetric form:

$$\langle \mathbf{X}_i(\mathbf{r}') \mathbf{X}_j(\mathbf{r} + \mathbf{r}') \rangle_{\mathbf{r}'} = A \delta_{ij} + B \hat{r}_i \hat{r}_j + C \hat{\lambda}_i \hat{\lambda}_j + D (\hat{r}_i \hat{\lambda}_j + \hat{\lambda}_i \hat{r}_j) \quad (24)$$

Here, $\langle \dots \rangle_{\mathbf{r}'}$ denotes volume averaging over the 3D position vector \mathbf{r}' , and $\hat{\lambda} = \hat{B}$ is the mean field unit vector. Note that A, B, C, D are all functions of \mathbf{r} . Due to axis-symmetry, it suffices to write $\mathbf{r} = (r, \mu = \cos^{-1}(\hat{r} \cdot \hat{\lambda}))$. Similar expressions can be done in Fourier space with \hat{k} and $\hat{\lambda}$.

The axis-symmetric model can be further expressed using frame vectors. Mathematically, in the case when the frame vectors are orthogonal, denoted as $(\hat{\zeta}^A, \hat{\zeta}^F, \hat{\zeta}^P)$ (see Tab.6), the traceless¹⁰ tensor of $\langle \tilde{\mathbf{X}}_i(\mathbf{k}') \tilde{\mathbf{X}}_j(\mathbf{k} + \mathbf{k}') \rangle_{\mathbf{k}'}$ in the Fourier space can be represented in a linear, separable form:

$$\langle \tilde{\mathbf{X}}_i(\mathbf{k}') \tilde{\mathbf{X}}_j(\mathbf{k} + \mathbf{k}') \rangle_{\mathbf{k}'} = C_A \hat{\zeta}^A \hat{\zeta}^A + C_F \hat{\zeta}^F \hat{\zeta}^F + C_P \hat{\zeta}^P \hat{\zeta}^P \quad (25)$$

Here, $C_{A,F,P}$ are constants. Notably, for the case of X representing magnetic field fluctuations or velocity fluctuations in incompressible turbulence, $C_P = 0$, resulting in a highly simplified expression that is axis-symmetric.

When we observe Eq. 24 or Eq. 25 in observations, an additional anisotropy is introduced depending on how the line of sight is oriented relative to the frame vectors $(\hat{\zeta}^A, \hat{\zeta}^F, \hat{\zeta}^P)$ (Yuen et al, 2023c). Earlier studies (Zhang et al, 2020b) utilized this fact to quantify mode signatures in synchrotron polarization maps, while more recently (Malik et al, 2023) used the statistical relations to determine the line-of-sight angle. In Kandel et al (2016) and later Kandel et al (2017), they discussed how the anisotropy of both intensity and velocity

¹⁰i.e., removing the A-term, which occurs when the variable itself has a zero mean

centroid correlation functions (Eq. 24) is related to (a) mode fraction, (b) the underlying turbulence model, and (c) the inclination angle of the mean magnetic field relative to the line of sight. The full context of Kandel et al (2016, 2017) is beyond the scope of this article; however, we want to emphasize that the geometric relations are not simple linear or monotonic functions of the three dependencies (a-c) we listed above (see also Lazarian et al (2022b) for more examples).

3.3.2 Velocity Channel map and velocity caustics

Perhaps the most important observation quantity for HI emission map is the velocity channel map. In Lazarian and Pogosyan (2000) it was analytically described how the density and velocity fluctuations contribute to the fluctuation of velocity channels. The density in PPV space of emitters with temperature T moving along the line-of-sight with stochastic turbulent velocity $v_{turb}(\mathbf{x})$ and regular coherent velocity $v_g(\mathbf{x})$ is (See Lazarian and Pogosyan 2004):

$$p(\mathbf{X}, v_0, \Delta v) = \int dz \rho(\mathbf{X}, z) \left(\frac{m}{2\pi k_B T} \right)^{1/2} \times \int_{v_0 - \Delta v/2}^{v_0 + \Delta v/2} dv W(v) e^{-\frac{m(v - v_{turb}(\mathbf{X}, z))^2}{2k_B T(\mathbf{X}, z)}}, \quad (26)$$

where sky position is described by 2D vector $\mathbf{X} = (x, y)$ and z is the line-of-sight coordinate and $W(v)$ is a window function given by the instrument. Formally we can always write the fluctuation of velocity channel intensity as:

$$p(\mathbf{X}, v_0, \Delta v) - \langle p \rangle_{\mathbf{X} \in A} = p_d(\mathbf{X}, v_0, \Delta v) + p_v(\mathbf{X}, v_0, \Delta v) \quad (27)$$

where $\langle p \rangle_{\mathbf{X} \in A}$ represents the velocity channel averaged over a certain spatial area A . The subtraction of the mean value in Eq.27 is required as we deal with the fluctuations arising from turbulence. Notice that p_d and p_v are functions of the Plane of Sky (POS) two dimensional vector \mathbf{X} , as well as the velocity channel position v_0 and channel width Δv . In what follows, we shall refer to p_v , i.e. the velocity contribution to velocity channels, as the **velocity caustics contribution**. It is noted by Lazarian and Pogosyan (2000) that in the case of thin ($\Delta v \ll 1$) channel map is dominated by velocity fluctuations. A cartoon from Yuen et al (2021) summarizes the science behind the velocity caustics fluctuations (Fig.12).

There was a proposal (Clark et al, 2019) that utilized a 128^3 isothermal simulation and a statistically unnormalized parameter (See criticism from Yuen et al 2019) to claim that the fluctuations from channel maps arise from density fluctuations from cold neutral media, which was also taken for granted by Kalberla et al (2022). It was revealed by a systematic study by Yuen et al (2021) that the velocity and density fluctuations can be separated in channel maps and they can have a varying fraction depending on the turbulence properties.

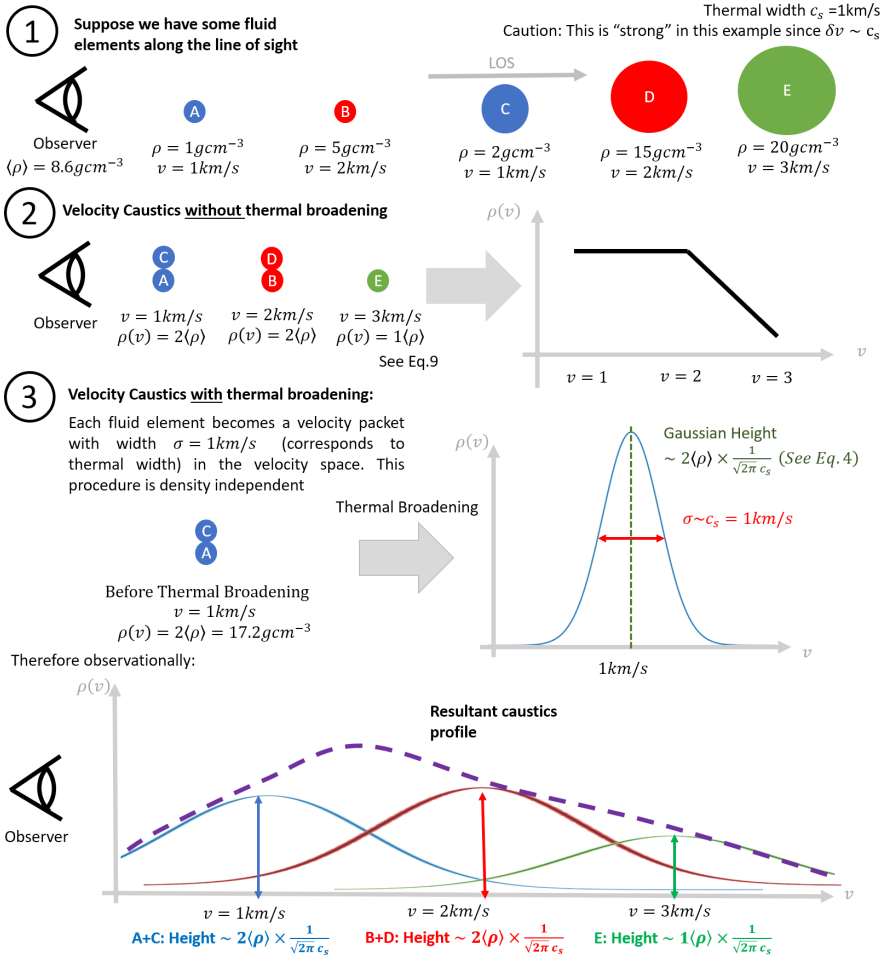


Fig. 12 A cartoon illustrating how velocity caustics are formed in a spectroscopic position-velocity (PPV) cube and the concept of velocity and density fluctuations in PPV data. From the top: Panel (1) shows our example that facilitates the discussion of velocity caustics. Panel (2): We show how the velocity caustics, based on the example in (1), look like without thermal broadening. Panel (3): The velocity caustics with thermal broadening, in the view of the $\rho(v) - v$ diagram, where we plot the caustics profile (the purple dashed line) as a function of v . From [Yuen et al \(2021\)](#).

Summarized by [Yuen et al \(2021\)](#), there are several properties that the density (p_d) and velocity (p_v) contributions obey:

1. Orthogonality of p_d and p_v when $M_s \ll 1$
2. $p_v = 0$ when $\Delta v \rightarrow \infty$
3. $p_d \propto I$ when $M_s \ll 1$

With these items, [Yuen et al \(2021\)](#) created the Velocity Decomposition Algorithm (VDA) which derived analytically the formula for p_v and p_d which

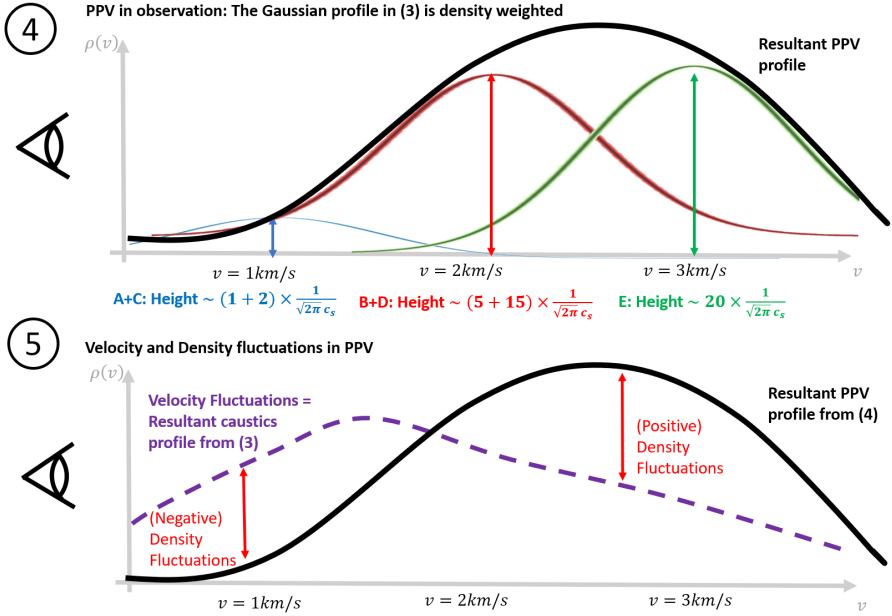


Fig. 13 (continuing Fig.12). Panel (4): The real PPV profile in observations (the black line) according to our example in panel (1). Panel (5): The differences between the caustics profile and the true PPV profile correspond to the density fluctuation, while the caustics profile itself represents the velocity fluctuation. From [Yuen et al \(2021\)](#).

enables the extraction of density and velocity fluctuations in channel maps:

$$p_v = p - (\langle pI \rangle - \langle p \rangle \langle I \rangle) \frac{I - \langle I \rangle}{\sigma_I^2}$$

$$p_d = p - p_v \quad (28)$$

$$= (\langle pI \rangle - \langle p \rangle \langle I \rangle) \frac{I - \langle I \rangle}{\sigma_I^2}$$

An observational application of Eq.28 and the statistical analysis is shown in Fig.14. It is evident from Fig.14 that: (i) The velocity caustics contribution is never zero and is spatially uncorrelated to density features. (ii) The relative contribution of density and velocity contribution is a function of channel width, particularly in the thin channel case where it is the fluctuations of velocity that give rise to filamentary features in the channel map.

What is the impact of [Yuen et al \(2021\)](#) for the study of filaments in HI emission maps? It is evident that if the channel map is velocity-like (i.e. $\langle p_v^2 \rangle > \langle p_d^2 \rangle$ in Eq.28), then the GS95 of filaments (c.f. [Xu et al 2019](#), Eq.13,14) can be directly applied without consideration of complicated density processes, as we discussed in Section 3.1.2. Furthermore, by varying the channel width, we can obtain both velocity and density statistics of filaments, allowing us to directly compare them with the multiphase physics as outlined in Section 3.2.

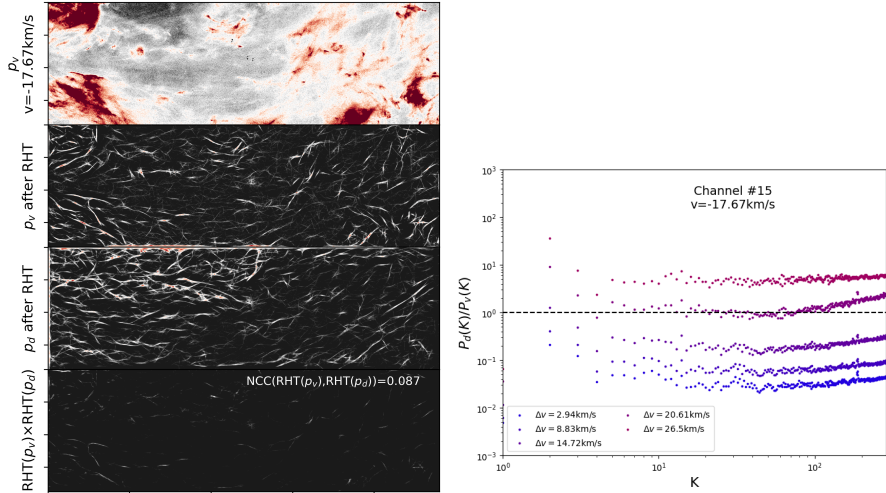


Fig. 14 Left panel: A set of figures showing how a selected wing channel ($v = -17.67 \text{ km/s}$, $\Delta v = 2.94 \text{ km/s}$) from the region in Clark et al (2015) would look like after Velocity Decomposition Algorithm (VDA, Yuen et al 2021), and the output of RHT from VDA maps. From the top panel: The p_v map after VDA. 2nd and 3rd panels from the top: The RHT results of p_v and p_d , respectively, scaled to $[0, 1]$. The lower panel: The product of the RHT results of p_d and p_v , scaled to $[0, 1]$. The normalized correlation coefficient ($NCC(A, B) = \frac{\langle (A - \langle A \rangle)(B - \langle B \rangle) \rangle}{\sigma_A \sigma_B}$, see Yuen et al (2019), $NCC \in [-1, 1]$) is 0.087, which means the RHT results of p_d and p_v are basically uncorrelated. Right panel: The spectra ratio P_d/P_v at the wing channel from the HI data from Clark et al (2015) at $v = -17.67 \text{ km/s}$ and $\Delta v = 2.94 \text{ km/s}$. We can see that as the channel width goes smaller, the spectra ratio quickly drops below one for most K . From Yuen et al (2021).

3.3.3 HI Absorption, and HI-H₂ Chemistry

The effect of absorption (Seifried et al, 2020b) and HI-H₂ conversion (Bialy and Sternberg, 2016; Beuther et al, 2016; Bialy et al, 2017; Gong et al, 2023) creates extra complications in deciphering how the emission map of HI looks and how to interpret the filamentary features therein. In this section, we provide a brief highlight of how these two effects contribute to the observational appearance of HI.

As discussed in Section 3.1, features with high density, low β , and a high sonic Mach number preferentially align perpendicular to the magnetic field. This alignment is well observed in simulations of both isothermal (e.g., Kowal and Lazarian 2010; Lazarian and Yuen 2018b) and multiphase media (Kritsuk et al 2018; Yuen et al 2021; Ho et al 2023). However, these high-density features are essentially unseen in observational HI emission maps (Clark et al, 2014, 2015; Kalberla et al, 2017; Kalberla and Haud, 2018). To address this issue, two primary mechanisms lower the emission strength of ultra-dense ($> \sim 50 \text{ cm}^{-3}$) cold neutral media: the high optical depth of cold neutral media and the sharp HI - H₂ conversion density threshold, causing these ultra-dense features to

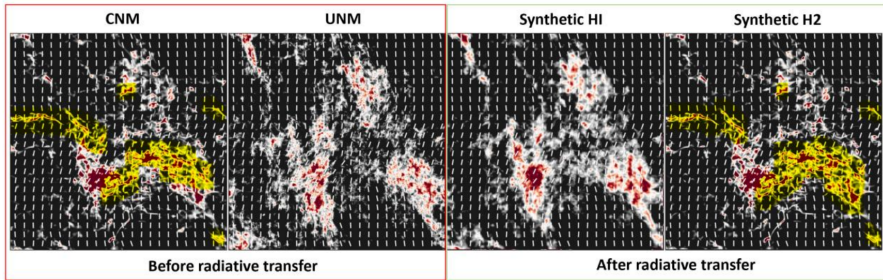


Fig. 15 (Left 2 panels) A set of figures shows how the actual distributions of CNM (far left) and UNM (second left) column densities look like in our multiphase simulation before radiative transfer after 20 Myr has passed in simulations (right two panels). We perform an observational synthesis and produce the synthetic HI column densities (second right) and the H2 column densities (far right) overlaid with the projected B-field (white vector). One can see that both CNM and synthetic H2 have a significant portion of features being perpendicular to the B-field (yellow region). However, for UNM and synthetic HI map, they have almost zero perpendicular features. Modified from [Yuen et al \(2021\)](#).

convert to H2 and become dark at 21cm lines. [Seifried et al \(2020a\)](#) discusses how self-absorption of HI favors the presence of field-parallel filaments in observational maps.

An additional effect is the HI-H2 conversion, where [Bialy and Sternberg \(2016\)](#) showed that the transition from HI to H2 occurs rapidly, with one species dropping by an order of magnitude in density when the density increases. We can model this transition via radiative transfer processes by incorporating arguments related to both optical depth and HI-H2 conversion. [Fig. 15](#) illustrates the synthetic results due to these optical effects. From this figure, it becomes evident that most of the features perpendicular to the magnetic field are extinguished in synthetic HI emission maps due to the combined effects of HI-H2 transition and high optical depth.

4 Summary and conclusions

In Section 1, we posed two key questions:

1. **Why are observed CNM filaments only parallel to the magnetic field while simulations contain both parallel and perpendicular orientations?**

Filaments form naturally in MHD turbulence, regardless of the phases. In the case of isothermal supersonic low β MHD turbulence (Section 3.1), there are typically two types of density enhancements: parallel (to magnetic field) filaments which have lower density, and perpendicular filaments which have higher density. These filaments are relatively stable in isothermal turbulence (in timescales of eddy over time) but thermal instabilities cause long filaments to fragment.

Thermal instabilities occur when the presence of radiative heating and cooling creates a nontrivial equation of state (Section 3.2, i.e. $P \propto \rho^n$ with $n < 0$), in which the pressure term at a certain range of densities becomes gravity-like instead of supportive. As a result, long perpendicular filaments are fragmented into smaller pieces in timescales shorter than the eddy turnover time. Multiphase MHD turbulence simulation shows that perpendicular filaments that have densities nearing the cold phase are thermally unstable. As a result, the perpendicular filaments are less extended on the sky *provided that the gas tracers could see the entire density ranges of multiphase interstellar turbulence*.

Observational constraints of 21 cm lines further complicates the CNM seen in interferometric measurements (Section 3.3). CNM becomes optically thick and preferentially perpendicular to magnetic fields right at its own density threshold. As a result, 21 cm measurements traces only the optical thin, long filamentary features that are preferentially parallel to magnetic field, but the perpendicular filaments are self-absorbed. Furthermore, the HI-H2 conversion becomes very effective right after the formation of CNM. The perpendicular filaments are therefore mostly converted to molecular hydrogen, which are dark in 21 cm lines.

The channel map effect (Section 3.3) also creates additional impact to the relative ratio of parallel and perpendicular filaments seen in observations. Velocity crowding effect in the presence of turbulence generates filamentary features in channel map, despite no real physical density enhancements. Unlike density fluctuations, turbulent velocity fluctuations are mostly parallel to magnetic field even in the case of supersonic limit. As a result, the amount of parallel filaments observed in 21cm lines are significantly increased due to velocity crowding. The effect of velocity crowding can be diminished by the Velocity Decomposition Algorithm.

2. **Why does observed HI have an aspect ratio of hundreds while simulations do not?**

As previously explained the long aspect ratio observed in HI filaments are likely attributed to algorithmic effects, projection effects, and the conflation of velocity and density fluctuations in H1 channel maps.

The filament detection method (Section 2) together with the velocity crowding effect (Section 3.3) will create illusory aspect ratios of filaments. Filaments that are next to each other, oriented in the same way and classified with edge detection method are likely be identified as a thin filament with high aspect ratio (Section 3.1). As we have outlined both algorithmically (Section 2) and analytically (Section 3.1, 3.3), observed 21 cm lines are subjected to numerous effects along the line of sight, on top of the true physical effects from turbulence and thermal instabilities. Determining whether the filamentary structures observed in channel map or intensity maps are really true filaments, sub-structures from a larger system, or artifacts is necessary before seeking physical explanation of why filaments carry certain aspect ratios.

Filaments with large aspect ratios are generally not thermally stable. Turbulence plays a crucial role in extending and stabilizing the spatial and temporal properties of these fragmented filaments. The extended lifetime of unstable neutral medium (UNM), due to its lower Alfvénic mach number and its role as a thermal cushion, is essential for explaining why CNM does not rapidly dissipate by its supersonic turbulence. CNM, while not gravitationally bound, can persist stably before fully converting into H₂. The strong correlation between a high fraction of UNM and turbulence indicates that UNM fraction could serve as a turbulent diagnostic for statistical studies. Additional support by the heat transport effect due to turbulence anisotropy is explored in Section 3.2.4. However, how exactly the interplay between turbulence and heat transport impacts the aspect ratio of physical filaments is still a subject of research.

Despite significant advancements in observational and simulation capabilities, many mysteries surrounding the interstellar medium and its role in star formation persist. Ongoing efforts, such as large-scale simulations and observations, hold promise for shedding light on these questions and providing a deeper understanding of the interstellar medium and its influence on star formation processes. Notable endeavors in this direction include large-scale simulations (Kritsuk et al, 2018; Kim and Ostriker, 2018; Soler et al, 2019; Fielding et al, 2023) and observations (Peek et al, 2018; Kalberla and Haud, 2015b; Murray et al, 2018; Rybarczyk et al, 2022a,b; Dickey et al, 2022), which aim to uncover more precise properties of the interstellar medium and investigate its subsequent impact on star formation processes.

A Notations and abbreviations

Table 6 List of notations used in this review.

Parameter	Meaning
\mathbf{r}	3-D separation $\mathbf{x}_2 - \mathbf{x}_1$
\mathbf{R}	2-D separation $\mathbf{X}_2 - \mathbf{X}_1$
z	Line of sight (LOS) variable
\mathbf{x}	3-D position vector
\mathbf{X}	2-D position vector
l	Distance of the 3d separation
\mathcal{L}	Size of a turbulent cloud
L_{inj}	Turbulence injection scale
A	A(lfven)-type vector component
F	F-type vector component $= C$ -type
P	P(otential)-type vector component
$\rho(\mathbf{r})$	3-D Density
$\rho(\mathbf{X}, v)$	Emitters' intensity in the PPV space
B	3-D magnetic field
b_{turb}	Turbulent part of the magnetic field
B_{\perp}	Projected magnetic field
$B_{x,y}$	The x & y components of the magnetic field
Q, U	Stokes Q & U parameters
v	3-D velocity
C	Velocity Centroid
θ	Magnetic field angle
ϕ	Polarization angle
M_s	Sonic Mach number
M_A	Alfvenic Mach number
n	Adiabatic index
$\langle A \rangle_x$	average of the quantity A over variable x
γ	Angle between the line of sight and symmetry axis
μ	$= \hat{k} \cdot \hat{B}$, $\mu = \cos(\gamma)$
$O(n)$	Big-O notation

Table 7 List of abbreviations used in this review, in alphabetical order

Abbreviations	Full name
CNM	Cold Neutral Media
GS95	Goldreich and Sridhar (1995)
MHD	Magneto-hydrodynamics
H_2	Molecular Hydrogen
HI	Neutral Hydrogen
HII	Ionized Hydrogen
LP	Lazarian & Pogosyan series (See Lazarian and Pogosyan (2000))
RHT	Rolling Hough Transform (See Clark et al 2015)
SNR	Signal to Noise
UNM	Unstable Neutral Media
USM	Unsharp Mask
VDA	Velocity Decomposition Algorithm (See Yuen et al 2021)
VGT	Velocity Gradient Technique (See Yuen and Lazarian 2017b)
WNM	Warm Neutral Media

Acknowledgment Inspiring discussions with Edouard Audit, Alex Lazarian, Alexei Kritsuk, and Chris McKee are acknowledged. Research presented in this article was supported by LANL LDRD-20220700PRD1. We also thank our collaborators who made much of the science discussed in this paper possible. KHY would like to thank the AAPPs-DPP committee for the invitation to deliver a talk on the subject and to write this review paper..

Conflict of Interest On behalf of all authors, the corresponding author states that there is no conflict of interest.

References

- Alina D, Shomanov A, Baimukhametova S (2022) MaLeFiSenta: Machine Learning for FilamentS Identification and orientation in the ISM. arXiv e-prints arXiv:2205.00683. <https://doi.org/10.48550/arXiv.2205.00683>, <https://arxiv.org/abs/2205.00683> [astro-ph.IM]
- Andersson BG, Lazarian A, Vaillancourt JE (2015) Interstellar Dust Grain Alignment. *ARA&A*53:501–539. <https://doi.org/10.1146/annurev-astro-082214-122414>
- André P, Di Francesco J, Ward-Thompson D, et al (2014) From Filamentary Networks to Dense Cores in Molecular Clouds: Toward a New Paradigm for Star Formation. In: Beuther H, Klessen RS, Dullemond CP, et al (eds) *Protostars and Planets VI*, pp 27–51, https://doi.org/10.2458/azu_uapress-9780816531240-ch002, 1312.6232
- Arzoumanian D, André P, Könyves V, et al (2019) Characterizing the properties of nearby molecular filaments observed with Herschel. *A&A*621:A42. <https://doi.org/10.1051/0004-6361/201832725>, <https://arxiv.org/abs/1810.00721> [astro-ph.GA]
- Audit E, Hennebelle P (2005) Thermal condensation in a turbulent atomic hydrogen flow. *A&A*433(1):1–13. <https://doi.org/10.1051/0004-6361:20041474>, <https://arxiv.org/abs/astro-ph/0410062> [astro-ph]
- Batchelor GK (1946) The Theory of Axisymmetric Turbulence. *Proceedings of the Royal Society of London Series A* 186(1007):480–502. <https://doi.org/10.1098/rspa.1946.0060>
- Beaumont CN, Offner SSR, Shetty R, et al (2013) Quantifying Observational Projection Effects Using Molecular Cloud Simulations. *ApJ*777(2):173. <https://doi.org/10.1088/0004-637X/777/2/173>, <https://arxiv.org/abs/1310.1929> [astro-ph.GA]
- Beuther H, Ragan SE, Johnston K, et al (2015) Filament fragmentation in high-mass star formation. *A&A*584:A67. <https://doi.org/10.1051/>

0004-6361/201527108, <https://arxiv.org/abs/1510.07063> [astro-ph.GA]

Beuther H, Bihl S, Rugel M, et al (2016) The HI/OH/Recombination line survey of the inner Milky Way (THOR). Survey overview and data release 1. *A&A*595:A32. <https://doi.org/10.1051/0004-6361/201629143>, <https://arxiv.org/abs/1609.03329> [astro-ph.GA]

Bialy S, Sternberg A (2016) Analytic H I-to-H₂ Photodissociation Transition Profiles. *ApJ*822(2):83. <https://doi.org/10.3847/0004-637X/822/2/83>, <https://arxiv.org/abs/1601.02608> [astro-ph.GA]

Bialy S, Bihl S, Beuther H, et al (2017) H I-to-H₂ Transition Layers in the Star-forming Region W43. *ApJ*835(2):126. <https://doi.org/10.3847/1538-4357/835/2/126>, <https://arxiv.org/abs/1612.02428> [astro-ph.GA]

Bonnaire T, Aghanim N, Decelle A, et al (2020) T-ReX: a graph-based filament detection method. *A&A*637:A18. <https://doi.org/10.1051/0004-6361/201936859>, <https://arxiv.org/abs/1912.00732> [astro-ph.CO]

Bonne L, Bontemps S, Schneider N, et al (2020) Formation of the Musca filament: evidence for asymmetries in the accretion flow due to a cloud-cloud collision. *A&A*644:A27. <https://doi.org/10.1051/0004-6361/202038281>, <https://arxiv.org/abs/2010.12479> [astro-ph.GA]

Brandenburg A, Lazarian A (2013) Astrophysical Hydromagnetic Turbulence. *Space Science Review*178(2-4):163–200. <https://doi.org/10.1007/s11214-013-0009-3>, <https://arxiv.org/abs/1307.5496> [astro-ph.SR]

Brunetti G, Lazarian A (2007) Compressible turbulence in galaxy clusters: physics and stochastic particle re-acceleration. *MNRAS*378(1):245–275. <https://doi.org/10.1111/j.1365-2966.2007.11771.x>, <https://arxiv.org/abs/astro-ph/0703591> [astro-ph]

Burkhart B, Lazarian A, Goodman A, et al (2013a) Hierarchical Structure of Magnetohydrodynamic Turbulence in Position-position-velocity Space. *ApJ*770(2):141. <https://doi.org/10.1088/0004-637X/770/2/141>, <https://arxiv.org/abs/1206.4703> [astro-ph.GA]

Burkhart B, Lazarian A, Ossenkopf V, et al (2013b) The Turbulence Power Spectrum in Optically Thick Interstellar Clouds. *ApJ*771(2):123. <https://doi.org/10.1088/0004-637X/771/2/123>, <https://arxiv.org/abs/1305.3619> [astro-ph.GA]

Chandran BDG (2000) Scattering of Energetic Particles by Anisotropic Magnetohydrodynamic Turbulence with a Goldreich-Sridhar Power Spectrum. *PRL*85(22):4656–4659. <https://doi.org/10.1103/PhysRevLett.85.4656>, <https://arxiv.org/abs/astro-ph/0008498> [astro-ph]

- Chandrasekhar S (1950) The Theory of Axisymmetric Turbulence. *Philosophical Transactions of the Royal Society of London Series A* 242(855):557–577. <https://doi.org/10.1098/rsta.1950.0010>
- Chen CY, Ostriker EC (2015) Anisotropic Formation of Magnetized Cores in Turbulent Clouds. *ApJ*810(2):126. <https://doi.org/10.1088/0004-637X/810/2/126>, <https://arxiv.org/abs/1508.02710> [astro-ph.GA]
- Chepurnov A, Lazarian A (2009) Turbulence Spectra from Doppler-Broadened Spectral Lines: Tests of the Velocity Channel Analysis and Velocity Coordinate Spectrum Techniques. *ApJ*693(2):1074–1083. <https://doi.org/10.1088/0004-637X/693/2/1074>, <https://arxiv.org/abs/astro-ph/0611463> [astro-ph]
- Chepurnov A, Lazarian A (2010) Extending the Big Power Law in the Sky with Turbulence Spectra from Wisconsin H α Mapper Data. *ApJ*710(1):853–858. <https://doi.org/10.1088/0004-637X/710/1/853>, <https://arxiv.org/abs/0905.4413> [astro-ph.GA]
- Chitsazzadeh S, Houde M, Hildebrand RH, et al (2012) Characterization of Turbulence from Submillimeter Dust Emission. *ApJ*749(1):45. <https://doi.org/10.1088/0004-637X/749/1/45>, <https://arxiv.org/abs/1202.1023> [astro-ph.GA]
- Cho J, Lazarian A (2002) Compressible Sub-Alfvénic MHD Turbulence in Low- β Plasmas. *PRL*88(24):245001. <https://doi.org/10.1103/PhysRevLett.88.245001>, <https://arxiv.org/abs/astro-ph/0205282> [astro-ph]
- Cho J, Lazarian A (2003) Compressible magnetohydrodynamic turbulence: mode coupling, scaling relations, anisotropy, viscosity-damped regime and astrophysical implications. *MNRAS*345(12):325–339. <https://doi.org/10.1046/j.1365-8711.2003.06941.x>, <https://arxiv.org/abs/astro-ph/0301062> [astro-ph]
- Cho J, Lazarian A (2004) Thermal Conduction in Magnetized Turbulent Gas. *Journal of Korean Astronomical Society* 37(5):557–562. <https://doi.org/10.5303/JKAS.2004.37.5.557>
- Cho J, Lazarian A (2005) Generation of compressible modes in MHD turbulence. *Theoretical and Computational Fluid Dynamics* 19(2):127–157. <https://doi.org/10.1007/s00162-004-0157-x>
- Cho J, Vishniac ET (2000) The Anisotropy of Magnetohydrodynamic Alfvénic Turbulence. *ApJ*539(1):273–282. <https://doi.org/10.1086/309213>, <https://arxiv.org/abs/astro-ph/0003403> [astro-ph]
- Cho J, Lazarian A, Honein A, et al (2003) Thermal Conduction in Magnetized Turbulent Gas. *ApJL*589(2):L77–L80. <https://doi.org/10.1086/>

376492, <https://arxiv.org/abs/astro-ph/0302503> [astro-ph]

- Choi E, Stone JM (2012) The Effect of Anisotropic Conduction on the Thermal Instability in the Interstellar Medium. *ApJ*747(2):86. <https://doi.org/10.1088/0004-637X/747/2/86>, <https://arxiv.org/abs/1112.4841> [astro-ph.GA]
- Clark SE, Hensley BS (2019) Mapping the Magnetic Interstellar Medium in Three Dimensions over the Full Sky with Neutral Hydrogen. *ApJ*887(2):136. <https://doi.org/10.3847/1538-4357/ab5803>, <https://arxiv.org/abs/1909.11673> [astro-ph.GA]
- Clark SE, Peek JEG, Putman ME (2014) Magnetically Aligned H I Fibers and the Rolling Hough Transform. *ApJ*789(1):82. <https://doi.org/10.1088/0004-637X/789/1/82>, <https://arxiv.org/abs/1312.1338> [astro-ph.GA]
- Clark SE, Hill JC, Peek JEG, et al (2015) Neutral Hydrogen Structures Trace Dust Polarization Angle: Implications for Cosmic Microwave Background Foregrounds. *PRL*115(24):241302. <https://doi.org/10.1103/PhysRevLett.115.241302>, <https://arxiv.org/abs/1508.07005> [astro-ph.CO]
- Clark SE, Peek JEG, Miville-Deschênes MA (2019) The Physical Nature of Neutral Hydrogen Intensity Structure. *ApJ*874(2):171. <https://doi.org/10.3847/1538-4357/ab0b3b>, <https://arxiv.org/abs/1902.01409> [astro-ph.GA]
- Colombo D, König C, Urquhart JS, et al (2021) OGHReS: Large-scale filaments in the outer Galaxy. *A&A*655:L2. <https://doi.org/10.1051/0004-6361/202142182>, <https://arxiv.org/abs/2111.02768> [astro-ph.GA]
- Commerçon B, Marcowith A, Dubois Y (2019) Cosmic-ray propagation in the bi-stable interstellar medium. I. Conditions for cosmic-ray trapping. *A&A*622:A143. <https://doi.org/10.1051/0004-6361/201833809>, <https://arxiv.org/abs/1811.11509> [astro-ph.GA]
- Crutcher RM, Wandelt B, Heiles C, et al (2010) Magnetic Fields in Interstellar Clouds from Zeeman Observations: Inference of Total Field Strengths by Bayesian Analysis. *ApJ*725(1):466–479. <https://doi.org/10.1088/0004-637X/725/1/466>
- Dickey JM, Dempsey JM, Pingel NM, et al (2022) GASKAP Pilot Survey Science. II. ASKAP Zoom Observations of Galactic 21 cm Absorption. *ApJ*926(2):186. <https://doi.org/10.3847/1538-4357/ac3a89>, <https://arxiv.org/abs/2111.04545> [astro-ph.GA]
- Dolginov AZ, Mytrophanov IG (1976) Orientation of Cosmic Dust Grains (In Russian). *Astrophysics and Space Science*43:257. <https://doi.org/10.1007/BF00640009>

Draine BT (2011) *Physics of the Interstellar and Intergalactic Medium*

Draine BT, Weingartner JC (1996) Alignment of Interstellar Grains by Starlight. In: American Astronomical Society Meeting Abstracts, p 16.02

Esquivel A, Lazarian A (2005) Velocity Centroids as Tracers of the Turbulent Velocity Statistics. *ApJ*631(1):320–350. <https://doi.org/10.1086/432458>, <https://arxiv.org/abs/astro-ph/0401603> [astro-ph]

Federrath C, Roman-Duval J, Klessen RS, et al (2010) Comparing the statistics of interstellar turbulence in simulations and observations. Solenoidal versus compressive turbulence forcing. *A&A*512:A81. <https://doi.org/10.1051/0004-6361/200912437>, <https://arxiv.org/abs/0905.1060> [astro-ph.SR]

Field GB (1965) Thermal Instability. *ApJ*142:531. <https://doi.org/10.1086/148317>

Fielding DB, Ripperda B, Philippov AA (2023) Plasmoid Instability in the Multiphase Interstellar Medium. *ApJL*949(1):L5. <https://doi.org/10.3847/2041-8213/accf1f>, <https://arxiv.org/abs/2211.06434> [astro-ph.GA]

Fissel LM, Ade PAR, Angilè FE, et al (2016) Balloon-Borne Submillimeter Polarimetry of the Vela C Molecular Cloud: Systematic Dependence of Polarization Fraction on Column Density and Local Polarization-Angle Dispersion. *ApJ*824(2):134. <https://doi.org/10.3847/0004-637X/824/2/134>, <https://arxiv.org/abs/1509.05298> [astro-ph.GA]

Gaensler BM, Haverkorn M, Burkhart B, et al (2011) Low-Mach-number turbulence in interstellar gas revealed by radio polarization gradients. *Nat*478(7368):214–217. <https://doi.org/10.1038/nature10446>, <https://arxiv.org/abs/1110.2896> [astro-ph.GA]

Gazol A, Vázquez-Semadeni E, Sánchez-Salcedo FJ, et al (2001) The Temperature Distribution in Turbulent Interstellar Gas. *ApJL*557(2):L121–L124. <https://doi.org/10.1086/322873>, <https://arxiv.org/abs/astro-ph/0105342> [astro-ph]

Goldreich P, Sridhar S (1995) Toward a Theory of Interstellar Turbulence. II. Strong Alfvénic Turbulence. *ApJ*438:763. <https://doi.org/10.1086/175121>

Gómez GC, Vázquez-Semadeni E (2014) Filaments in Simulations of Molecular Cloud Formation. *ApJ*791(2):124. <https://doi.org/10.1088/0004-637X/791/2/124>, <https://arxiv.org/abs/1308.6298> [astro-ph.GA]

Gong M, Ho KW, Stone JM, et al (2023) Implementation of Chemistry in the Athena++ Code. *ApJS*268(2):42. <https://doi.org/10.3847/1538-4365/aceaf9>, <https://arxiv.org/abs/2305.04965> [astro-ph.GA]

- González-Casanova DF, Lazarian A (2017) Velocity Gradients as a Tracer for Magnetic Fields. *ApJ*835(1):41. <https://doi.org/10.3847/1538-4357/835/1/41>, <https://arxiv.org/abs/1608.06867> [astro-ph.GA]
- Hacar A, Clark SE, Heitsch F, et al (2023) Initial Conditions for Star Formation: a Physical Description of the Filamentary ISM. In: Inutsuka S, Aikawa Y, Muto T, et al (eds) *Protostars and Planets VII*, p 153, <https://doi.org/10.48550/arXiv.2203.09562>, 2203.09562
- Heiles C (2001) New Temperatures of Diffuse Interstellar Gas: Thermally Unstable Gas. *ApJL*551(1):L105–L108. <https://doi.org/10.1086/319844>, <https://arxiv.org/abs/astro-ph/0103126> [astro-ph]
- Heiles C, Troland TH (2003) The Millennium Arecibo 21 Centimeter Absorption-Line Survey. II. Properties of the Warm and Cold Neutral Media. *ApJ*586(2):1067–1093. <https://doi.org/10.1086/367828>, <https://arxiv.org/abs/astro-ph/0207105> [astro-ph]
- Hennebelle P (2013) On the origin of non-self-gravitating filaments in the ISM. *A&A*556:A153. <https://doi.org/10.1051/0004-6361/201321292>, <https://arxiv.org/abs/1306.5452> [astro-ph.GA]
- Hennebelle P, Audit E (2007) On the structure of the turbulent interstellar atomic hydrogen. I. Physical characteristics. Influence and nature of turbulence in a thermally bistable flow. *A&A*465(2):431–443. <https://doi.org/10.1051/0004-6361:20066139>, <https://arxiv.org/abs/astro-ph/0612778> [astro-ph]
- Hennebelle P, Audit E, Miville-Deschênes MA (2007) On the structure of the turbulent interstellar atomic hydrogen. II. First comparison between observation and theory. Are the characteristics of molecular clouds determined early in the turbulent 2-phase atomic gas? *A&A*465(2):445–456. <https://doi.org/10.1051/0004-6361:20066141>
- Heyer M, Gong H, Ostriker E, et al (2008) Magnetically Aligned Velocity Anisotropy in the Taurus Molecular Cloud. *ApJ*680(1):420–427. <https://doi.org/10.1086/587510>, <https://arxiv.org/abs/0802.2084> [astro-ph]
- Ho KW, Yuen KH, Lazarian A (2023) How the existence of unstable neutral media restricts the aspect ratio of cold neutral media? *MNRAS*521(1):230–240. <https://doi.org/10.1093/mnras/stad481>
- Hoang T, Lazarian A (2008) Radiative torque alignment: essential physical processes. *MNRAS*388(1):117–143. <https://doi.org/10.1111/j.1365-2966.2008.13249.x>, <https://arxiv.org/abs/0707.3645> [astro-ph]
- Hoang T, Lazarian A (2016) A Unified Model of Grain Alignment:

- Radiative Alignment of Interstellar Grains with Magnetic Inclusions. *ApJ*831(2):159. <https://doi.org/10.3847/0004-637X/831/2/159>, <https://arxiv.org/abs/1605.02828> [astro-ph.GA]
- Jackson JM, Finn SC, Chambers ET, et al (2010) The “Nessie” Nebula: Cluster Formation in a Filamentary Infrared Dark Cloud. *ApJL*719(2):L185–L189. <https://doi.org/10.1088/2041-8205/719/2/L185>, <https://arxiv.org/abs/1007.5492> [astro-ph.GA]
- Juvela M (2016) Template matching method for the analysis of interstellar cloud structure. *A&A*593:A58. <https://doi.org/10.1051/0004-6361/201628727>, <https://arxiv.org/abs/1607.01931> [astro-ph.IM]
- Kalberla PMW, Haud U (2015a) GASS: The Parkes Galactic All-Sky Survey. Update: improved correction for instrumental effects and new data release. *A&A*578:A78. <https://doi.org/10.1051/0004-6361/201525859>, <https://arxiv.org/abs/1505.01011> [astro-ph.GA]
- Kalberla PMW, Haud U (2015b) GASS: The Parkes Galactic All-Sky Survey. Update: improved correction for instrumental effects and new data release. *A&A*578:A78. <https://doi.org/10.1051/0004-6361/201525859>, <https://arxiv.org/abs/1505.01011> [astro-ph.GA]
- Kalberla PMW, Haud U (2018) Properties of cold and warm H I gas phases derived from a Gaussian decomposition of HI4PI data. *A&A*619:A58. <https://doi.org/10.1051/0004-6361/201833146>, <https://arxiv.org/abs/1806.04085> [astro-ph.GA]
- Kalberla PMW, Haud U (2019) Turbulent power distribution in the local interstellar medium. *A&A*627:A112. <https://doi.org/10.1051/0004-6361/201834533>, <https://arxiv.org/abs/1905.08583> [astro-ph.GA]
- Kalberla PMW, Kerp J, Haud U, et al (2016) Cold Milky Way HI Gas in Filaments. *ApJ*821(2):117. <https://doi.org/10.3847/0004-637X/821/2/117>, <https://arxiv.org/abs/1602.07604> [astro-ph.GA]
- Kalberla PMW, Kerp J, Haud U, et al (2017) H I anisotropies associated with radio-polarimetric filaments . Steep power spectra associated with cold gas. *A&A*607:A15. <https://doi.org/10.1051/0004-6361/201629627>, <https://arxiv.org/abs/1707.05672> [astro-ph.GA]
- Kalberla PMW, Kerp J, Haud U (2020) H I filaments are cold and associated with dark molecular gas. HI4PI-based estimates of the local diffuse CO-dark H₂ distribution. *A&A*639:A26. <https://doi.org/10.1051/0004-6361/202037602>, <https://arxiv.org/abs/2004.14630> [astro-ph.GA]
- Kalberla PMW, Kerp J, Haud U (2021) Local HI filaments driven by

- a small-scale dynamo. Unraveling the velocities and tangling of dusty magnetized structures. *A&A*654:A91. <https://doi.org/10.1051/0004-6361/202140274>, <https://arxiv.org/abs/2101.00273> [astro-ph.GA]
- Kalberla PMW, Kerp J, Haud U (2022) Correlations between turbulent velocity and density fields in the local interstellar medium. arXiv e-prints arXiv:2202.01610. <https://doi.org/10.48550/arXiv.2202.01610>, <https://arxiv.org/abs/2202.01610> [astro-ph.GA]
- Kandel D, Lazarian A, Pogosyan D (2016) Extending velocity channel analysis for studying turbulence anisotropies. *MNRAS*461(2):1227–1259. <https://doi.org/10.1093/mnras/stw1296>, <https://arxiv.org/abs/1604.06102> [astro-ph.GA]
- Kandel D, Lazarian A, Pogosyan D (2017) Study of velocity centroids based on the theory of fluctuations in position-position-velocity space. *MNRAS*464(3):3617–3635. <https://doi.org/10.1093/mnras/stw2512>, <https://arxiv.org/abs/1607.04316> [astro-ph.GA]
- Kim CG, Ostriker EC (2017) Three-phase Interstellar Medium in Galaxies Resolving Evolution with Star Formation and Supernova Feedback (TIGRESS): Algorithms, Fiducial Model, and Convergence. *ApJ*846(2):133. <https://doi.org/10.3847/1538-4357/aa8599>, <https://arxiv.org/abs/1612.03918> [astro-ph.GA]
- Kim CG, Ostriker EC (2018) Numerical Simulations of Multiphase Winds and Fountains from Star-forming Galactic Disks. I. Solar Neighborhood TIGRESS Model. *ApJ*853(2):173. <https://doi.org/10.3847/1538-4357/aaa5ff>, <https://arxiv.org/abs/1801.03952> [astro-ph.GA]
- Kim CG, Ostriker EC, Kim WT (2014) Three-dimensional Hydrodynamic Simulations of Multiphase Galactic Disks with Star Formation Feedback. II. Synthetic H I 21 cm Line Observations. *ApJ*786(1):64. <https://doi.org/10.1088/0004-637X/786/1/64>, <https://arxiv.org/abs/1403.5566> [astro-ph.GA]
- Kim CG, Ostriker EC, Raileanu R (2017) Superbubbles in the Multiphase ISM and the Loading of Galactic Winds. *ApJ*834(1):25. <https://doi.org/10.3847/1538-4357/834/1/25>, <https://arxiv.org/abs/1610.03092> [astro-ph.GA]
- Kim JG, Kim WT, Ostriker EC (2016) Disruption of Molecular Clouds by Expansion of Dusty H II Regions. *ApJ*819(2):137. <https://doi.org/10.3847/0004-637X/819/2/137>, <https://arxiv.org/abs/1601.03035> [astro-ph.GA]
- Kim JG, Kim WT, Ostriker EC (2018) Modeling UV Radiation Feedback from Massive Stars. II. Dispersal of Star-forming Giant Molecular Clouds by Photoionization and Radiation Pressure. *ApJ*859(1):68. <https://doi.org/10.3847/1538-4357/aabe27>, <https://arxiv.org/abs/1804.04664> [astro-ph.GA]

- Klessen RS, Glover SCO (2016) Physical Processes in the Interstellar Medium. Saas-Fee Advanced Course 43:85. https://doi.org/10.1007/978-3-662-47890-5_2, <https://arxiv.org/abs/1412.5182> [astro-ph.GA]
- Koch EW, Rosolowsky EW (2015) Filament identification through mathematical morphology. MNRAS452(4):3435–3450. <https://doi.org/10.1093/mnras/stv1521>, <https://arxiv.org/abs/1507.02289> [astro-ph.GA]
- Kolmogorov A (1941) The Local Structure of Turbulence in Incompressible Viscous Fluid for Very Large Reynolds' Numbers. Akademiia Nauk SSSR Doklady 30:301–305
- Kowal G, Lazarian A (2010) Velocity Field of Compressible Magneto-hydrodynamic Turbulence: Wavelet Decomposition and Mode Scalings. ApJ720(1):742–756. <https://doi.org/10.1088/0004-637X/720/1/742>, <https://arxiv.org/abs/1003.3697> [astro-ph.GA]
- Kowal G, Lazarian A, Beresnyak A (2007) Density Fluctuations in MHD Turbulence: Spectra, Intermittency, and Topology. ApJ658(1):423–445. <https://doi.org/10.1086/511515>, <https://arxiv.org/abs/astro-ph/0608051> [astro-ph]
- Kowal G, Lazarian A, Vishniac ET, et al (2012) Reconnection studies under different types of turbulence driving. Nonlinear Processes in Geophysics 19(2):297–314. <https://doi.org/10.5194/npg-19-297-2012>, <https://arxiv.org/abs/1203.2971> [astro-ph.SR]
- Koyama H, Inutsuka Si (2002) An Origin of Supersonic Motions in Interstellar Clouds. ApJL564(2):L97–L100. <https://doi.org/10.1086/338978>, <https://arxiv.org/abs/astro-ph/0112420> [astro-ph]
- Koyama H, Inutsuka Si (2004) The Field Condition: A New Constraint on Spatial Resolution in Simulations of the Nonlinear Development of Thermal Instability. ApJL602(1):L25–L28. <https://doi.org/10.1086/382478>, <https://arxiv.org/abs/astro-ph/0302126> [astro-ph]
- Kritsuk AG, Norman ML (2002) Thermal Instability-induced Interstellar Turbulence. ApJL569(2):L127–L131. <https://doi.org/10.1086/340785>, <https://arxiv.org/abs/astro-ph/0112437> [astro-ph]
- Kritsuk AG, Ustyugov SD, Norman ML (2017) The structure and statistics of interstellar turbulence. New Journal of Physics 19(6):065003. <https://doi.org/10.1088/1367-2630/aa7156>, <https://arxiv.org/abs/1705.01912> [astro-ph.GA]
- Kritsuk AG, Flauger R, Ustyugov SD (2018) Dust-Polarization Maps for Local Interstellar Turbulence. PRL121(2):021104. <https://doi.org/10.1103/PhysRevLett.121.021104>, <https://arxiv.org/abs/1711.11108> [astro-ph.GA]

- Kumar MSN, Palmeirim P, Arzoumanian D, et al (2020) Unifying low- and high-mass star formation through density-amplified hubs of filaments. The highest mass stars ($\lesssim 100 M_{\odot}$) form only in hubs. *A&A*642:A87. <https://doi.org/10.1051/0004-6361/202038232>, <https://arxiv.org/abs/2008.00295> [astro-ph.GA]
- Kunz MW, Bogdanović T, Reynolds CS, et al (2012) Buoyancy Instabilities in a Weakly Collisional Intracluster Medium. *ApJ*754(2):122. <https://doi.org/10.1088/0004-637X/754/2/122>, <https://arxiv.org/abs/1202.3442> [astro-ph.CO]
- Larson RB (1981) Turbulence and star formation in molecular clouds. *MNRAS*194:809–826. <https://doi.org/10.1093/mnras/194.4.809>
- Lazarian A (2006) Enhancement and Suppression of Heat Transfer by MHD Turbulence. *ApJL*645(1):L25–L28. <https://doi.org/10.1086/505796>, <https://arxiv.org/abs/astro-ph/0608045> [astro-ph]
- Lazarian A (2016) Damping of Alfvén Waves by Turbulence and Its Consequences: From Cosmic-ray Streaming to Launching Winds. *ApJ*833(2):131. <https://doi.org/10.3847/1538-4357/833/2/131>, <https://arxiv.org/abs/1607.02042> [astro-ph.HE]
- Lazarian A, Hoang T (2007) Radiative torques: analytical model and basic properties. *MNRAS*378(3):910–946. <https://doi.org/10.1111/j.1365-2966.2007.11817.x>, <https://arxiv.org/abs/0707.0886> [astro-ph]
- Lazarian A, Hoang T (2019) Magnetic Properties of Dust Grains, Effect of Precession, and Radiative Torque Alignment. *ApJ*883(2):122. <https://doi.org/10.3847/1538-4357/ab3d39>, <https://arxiv.org/abs/1810.10686> [astro-ph.GA]
- Lazarian A, Pogosyan D (2000) Velocity Modification of H I Power Spectrum. *ApJ*537(2):720–748. <https://doi.org/10.1086/309040>, <https://arxiv.org/abs/astro-ph/9901241> [astro-ph]
- Lazarian A, Pogosyan D (2004) Velocity Modification of the Power Spectrum from an Absorbing Medium. *ApJ*616(2):943–965. <https://doi.org/10.1086/422462>, <https://arxiv.org/abs/astro-ph/0405461> [astro-ph]
- Lazarian A, Pogosyan D (2006) Studying Turbulence Using Doppler-broadened Lines: Velocity Coordinate Spectrum. *ApJ*652(2):1348–1365. <https://doi.org/10.1086/508012>, <https://arxiv.org/abs/astro-ph/0511248> [astro-ph]
- Lazarian A, Pogosyan D (2008) Studying Velocity Turbulence from Doppler-broadened Absorption Lines: Statistics of Optical Depth Fluctuations. *ApJ*686(1):350–362. <https://doi.org/10.1086/591238>, <https://arxiv.org/abs/0707.0886>

[org/abs/0801.1151](https://arxiv.org/abs/0801.1151) [astro-ph]

Lazarian A, Pogoyan D (2012) Statistical Description of Synchrotron Intensity Fluctuations: Studies of Astrophysical Magnetic Turbulence. *ApJ*747(1):5. <https://doi.org/10.1088/0004-637X/747/1/5>, <https://arxiv.org/abs/1105.4617> [astro-ph.GA]

Lazarian A, Pogoyan D (2016) Spectrum and Anisotropy of Turbulence from Multi-frequency Measurement of Synchrotron Polarization. *ApJ*818(2):178. <https://doi.org/10.3847/0004-637X/818/2/178>, <https://arxiv.org/abs/1511.01537> [astro-ph.GA]

Lazarian A, Vishniac ET (1999) Reconnection in a Weakly Stochastic Field. *ApJ*517(2):700–718. <https://doi.org/10.1086/307233>, <https://arxiv.org/abs/astro-ph/9811037> [astro-ph]

Lazarian A, Yuen KH (2018a) Gradients of Synchrotron Polarization: Tracing 3D Distribution of Magnetic Fields. *ApJ*865(1):59. <https://doi.org/10.3847/1538-4357/aad3ca>, <https://arxiv.org/abs/1802.00028> [astro-ph.GA]

Lazarian A, Yuen KH (2018b) Tracing Magnetic Fields with Spectroscopic Channel Maps. *ApJ*853(1):96. <https://doi.org/10.3847/1538-4357/aaa241>, <https://arxiv.org/abs/1703.03119> [astro-ph.GA]

Lazarian A, Yuen KH, Lee H, et al (2017) Synchrotron Intensity Gradients as Tracers of Interstellar Magnetic Fields. *ApJ*842(1):30. <https://doi.org/10.3847/1538-4357/aa74c6>

Lazarian A, Yuen KH, Ho KW, et al (2018) Distribution of Velocity Gradient Orientations: Mapping Magnetization with the Velocity Gradient Technique. *ApJ*865(1):46. <https://doi.org/10.3847/1538-4357/aad7ff>, <https://arxiv.org/abs/1802.02984> [astro-ph.GA]

Lazarian A, Eyink GL, Jafari A, et al (2020) 3D turbulent reconnection: Theory, tests, and astrophysical implications. *Physics of Plasmas* 27(1):012305. <https://doi.org/10.1063/1.5110603>, <https://arxiv.org/abs/2001.00868> [astro-ph.HE]

Lazarian A, Yuen KH, Pogoyan D (2022a) arXiv e-prints

Lazarian A, Yuen KH, Pogoyan D (2022b) Magnetic Field Strength from Turbulence Theory. I. Using Differential Measure Approach. *ApJ*935(2):77. <https://doi.org/10.3847/1538-4357/ac6877>, <https://arxiv.org/abs/2204.09731> [astro-ph.GA]

Leurini S, Schisano E, Pillai T, et al (2019) Characterising the high-mass star forming filament G351.776-0.527 with Herschel and APEX dust continuum

- and gas observations. *A&A*21:A130. <https://doi.org/10.1051/0004-6361/201833612>, <https://arxiv.org/abs/1812.01035> [astro-ph.GA]
- Li C, Qiu K, Hu B, et al (2021) The Discovery of the Largest Gas Filament in Our Galaxy, or a New Spiral Arm? *ApJL*918(1):L2. <https://doi.org/10.3847/2041-8213/ac19bc>, <https://arxiv.org/abs/2108.01905> [astro-ph.GA]
- Li GX (2018) Scale-free gravitational collapse as the origin of $\rho \sim r^{-2}$ density profile - a possible role of turbulence in regulating gravitational collapse. *MNRAS*477(4):4951–4956. <https://doi.org/10.1093/mnras/sty657>, <https://arxiv.org/abs/1803.03273> [astro-ph.GA]
- Li HB, Henning T (2011) *Nature* 479:499
- Li Hb, Houde M, Lai Sp, et al (2010) Tracing Turbulent Ambipolar Diffusion in Molecular Clouds. *ApJ*718(2):905–912. <https://doi.org/10.1088/0004-637X/718/2/905>, <https://arxiv.org/abs/1003.2919> [astro-ph.SR]
- Li Hb, Fang M, Henning T, et al (2013) The link between magnetic fields and filamentary clouds: bimodal cloud orientations in the Gould Belt. *MNRAS*436(4):3707–3719. <https://doi.org/10.1093/mnras/stt1849>, <https://arxiv.org/abs/1310.6261> [astro-ph.GA]
- Li HB, Yuen KH, Otto F, et al (2015) Self-similar fragmentation regulated by magnetic fields in a region forming massive stars. *Nat*520(7548):518–521. <https://doi.org/10.1038/nature14291>, <https://arxiv.org/abs/1510.07094> [astro-ph.GA]
- Li HB, Jiang H, Fan X, et al (2017) The link between magnetic field orientations and star formation rates. *Nature Astronomy* 1:0158. <https://doi.org/10.1038/s41550-017-0158>, <https://arxiv.org/abs/1706.08452> [astro-ph.GA]
- Li Y, Gendron-Marsolais ML, Zhuravleva I, et al (2020) Direct Detection of Black Hole-driven Turbulence in the Centers of Galaxy Clusters. *ApJL*889(1):L1. <https://doi.org/10.3847/2041-8213/ab65c7>, <https://arxiv.org/abs/1911.06329> [astro-ph.GA]
- Liu J, Zhang Q, Liu HB, et al (2023) Deviation from a Continuous and Universal Turbulence Cascade in NGC 6334 due to Massive Star Formation Activity. *ApJ*949(1):30. <https://doi.org/10.3847/1538-4357/acc4c0>, <https://arxiv.org/abs/2303.08170> [astro-ph.GA]
- Maiti S, Makwana K, Zhang H, et al (2021) Cosmic ray Transport in Magnetohydrodynamic turbulence. arXiv e-prints arXiv:2108.01936. <https://arxiv.org/abs/2108.01936> [astro-ph.HE]
- Makwana KD, Yan H (2020) Properties of Magnetohydrodynamic Modes in

- Compressively Driven Plasma Turbulence. *Physical Review X* 10(3):031021. <https://doi.org/10.1103/PhysRevX.10.031021>, <https://arxiv.org/abs/1907.01853> [physics.plasm-ph]
- Malik S, Yuen KH, Yan H (2023) Diagnosis of 3D magnetic field and mode composition in MHD turbulence with Y-parameter. *MNRAS*524(4):6102–6113. <https://doi.org/10.1093/mnras/stad2225>, <https://arxiv.org/abs/2303.17282> [astro-ph.GA]
- Mallet A, Schekochihin AA, Chandran BDG (2015) Refined critical balance in strong Alfvénic turbulence. *MNRAS*449:L77–L81. <https://doi.org/10.1093/mnrasl/slv021>, <https://arxiv.org/abs/1406.5658> [astro-ph.SR]
- Maron J, Goldreich P (2001) Simulations of Incompressible Magnetohydrodynamic Turbulence. *ApJ*554(2):1175–1196. <https://doi.org/10.1086/321413>, <https://arxiv.org/abs/astro-ph/0012491> [astro-ph]
- Matthaeus WH, Smith C (1981) Structure of correlation tensors in homogeneous anisotropic turbulence. *Physical Review A* 24:2135–2144. <https://doi.org/10.1103/PhysRevA.24.2135>
- McClure-Griffiths NM, Dickey JM, Gaensler BM, et al (2006) Magnetically Dominated Strands of Cold Hydrogen in the Riegel-Crutcher Cloud. *ApJ*652(2):1339–1347. <https://doi.org/10.1086/508706>, <https://arxiv.org/abs/astro-ph/0608585> [astro-ph]
- McClure-Griffiths NM, Stanimirović S, Rybarczyk DR (2023) Atomic Hydrogen in the Milky Way: A Stepping Stone in the Evolution of Galaxies. *ARA&A*61:19–63. <https://doi.org/10.1146/annurev-astro-052920-104851>, <https://arxiv.org/abs/2307.08464> [astro-ph.GA]
- McKee CF, Ostriker EC (2007) Theory of Star Formation. *ARA&A*45(1):565–687. <https://doi.org/10.1146/annurev.astro.45.051806.110602>, <https://arxiv.org/abs/0707.3514> [astro-ph]
- McKee CF, Ostriker JP (1977) A theory of the interstellar medium: three components regulated by supernova explosions in an inhomogeneous substrate. *ApJ*218:148–169. <https://doi.org/10.1086/155667>
- Mocz P, Burkhart B (2018) Star formation from dense shocked regions in supersonic isothermal magnetoturbulence. *MNRAS*480(3):3916–3927. <https://doi.org/10.1093/mnras/sty1976>, <https://arxiv.org/abs/1805.11105> [astro-ph.GA]
- Murray CE, Stanimirović S, Goss WM, et al (2018) The 21-SPONGE H I Absorption Line Survey. I. The Temperature of Galactic H I. *ApJS*238(2):14. <https://doi.org/10.3847/1538-4365/aad81a>, <https://arxiv.org/abs/1805.11105>

[org/abs/1806.06065](https://arxiv.org/abs/1806.06065) [astro-ph.GA]

- Narayan R, Medvedev MV (2001) Thermal Conduction in Clusters of Galaxies. *ApJL*562(2):L129–L132. <https://doi.org/10.1086/338325>, <https://arxiv.org/abs/astro-ph/0110567> [astro-ph]
- Oughton S, Rädler KH, Matthaeus WH (1997) General second-rank correlation tensors for homogeneous magnetohydrodynamic turbulence. *Physical Review E* 56(3):2875–2888. <https://doi.org/10.1103/PhysRevE.56.2875>
- Padoan P, Juvela M, Kritsuk A, et al (2006) The Power Spectrum of Supersonic Turbulence in Perseus. *ApJL*653(2):L125–L128. <https://doi.org/10.1086/510620>, <https://arxiv.org/abs/astro-ph/0611248> [astro-ph]
- Padoan P, Nordlund Å, Kritsuk AG, et al (2007) Two Regimes of Turbulent Fragmentation and the Stellar Initial Mass Function from Primordial to Present-Day Star Formation. *ApJ*661(2):972–981. <https://doi.org/10.1086/516623>, <https://arxiv.org/abs/astro-ph/0701795> [astro-ph]
- Peek JEG, Babler BL, Zheng Y, et al (2018) The GALFA-H I Survey Data Release 2. *ApJS*234(1):2. <https://doi.org/10.3847/1538-4365/aa91d3>
- Pineda JE, Arzoumanian D, Andre P, et al (2023) From Bubbles and Filaments to Cores and Disks: Gas Gathering and Growth of Structure Leading to the Formation of Stellar Systems. In: Inutsuka S, Aikawa Y, Muto T, et al (eds) *Protostars and Planets VII*, p 233, <https://doi.org/10.48550/arXiv.2205.03935>, 2205.03935
- Rosolowsky EW, Pineda JE, Kauffmann J, et al (2008) Structural Analysis of Molecular Clouds: Dendrograms. *ApJ*679(2):1338–1351. <https://doi.org/10.1086/587685>, <https://arxiv.org/abs/0802.2944> [astro-ph]
- Rybarczyk DR, Gong M, Stanimirović S, et al (2022a) The Role of Neutral Hydrogen in Setting the Abundances of Molecular Species in the Milky Way’s Diffuse Interstellar Medium. II. Comparison between Observations and Theoretical Models. *ApJ*926(2):190. <https://doi.org/10.3847/1538-4357/ac4160>, <https://arxiv.org/abs/2112.05767> [astro-ph.GA]
- Rybarczyk DR, Stanimirović S, Gong M, et al (2022b) The Role of Neutral Hydrogen in Setting the Abundances of Molecular Species in the Milky Way’s Diffuse Interstellar Medium. I. Observational Constraints from ALMA and NOEMA. *ApJ*928(1):79. <https://doi.org/10.3847/1538-4357/ac5035>, <https://arxiv.org/abs/2109.06273> [astro-ph.GA]
- Scalo J, Elmegreen BG (2004) Interstellar Turbulence II: Implications and Effects. *ARA&A*42(1):275–316. <https://doi.org/10.1146/annurev.astro.42.120403.143327>, <https://arxiv.org/abs/astro-ph/0404452> [astro-ph]

- Schekochihin AA (2022) MHD turbulence: a biased review. *Journal of Plasma Physics* 88(5):155880501. <https://doi.org/10.1017/S0022377822000721>
- Seifried D, Haid S, Walch S, et al (2020a) SILCC-Zoom: H₂ and CO-dark gas in molecular clouds - the impact of feedback and magnetic fields. *MNRAS*492(1):1465–1483. <https://doi.org/10.1093/mnras/stz3563>, <https://arxiv.org/abs/1906.01015> [astro-ph.GA]
- Seifried D, Walch S, Weis M, et al (2020b) From parallel to perpendicular - On the orientation of magnetic fields in molecular clouds. *MNRAS*497(4):4196–4212. <https://doi.org/10.1093/mnras/staa2231>, <https://arxiv.org/abs/2003.00017> [astro-ph.GA]
- Seifried D, Beuther H, Walch S, et al (2022) On the accuracy of H I observations in molecular clouds - More cold H I than thought? *MNRAS*512(4):4765–4784. <https://doi.org/10.1093/mnras/stac607>, <https://arxiv.org/abs/2109.10917> [astro-ph.GA]
- Soler JD, Hennebelle P, Martin PG, et al (2013) An Imprint of Molecular Cloud Magnetization in the Morphology of the Dust Polarized Emission. *ApJ*774(2):128. <https://doi.org/10.1088/0004-637X/774/2/128>, <https://arxiv.org/abs/1303.1830> [astro-ph.GA]
- Soler JD, Beuther H, Rugel M, et al (2019) Histogram of oriented gradients: a technique for the study of molecular cloud formation. *A&A*622:A166. <https://doi.org/10.1051/0004-6361/201834300>, <https://arxiv.org/abs/1809.08338> [astro-ph.GA]
- Soler JD, Beuther H, Syed J, et al (2020) The history of dynamics and stellar feedback revealed by the H I filamentary structure in the disk of the Milky Way. *A&A*642:A163. <https://doi.org/10.1051/0004-6361/202038882>, <https://arxiv.org/abs/2007.07285> [astro-ph.GA]
- Sousbie T (2011) The persistent cosmic web and its filamentary structure - I. Theory and implementation. *MNRAS*414(1):350–383. <https://doi.org/10.1111/j.1365-2966.2011.18394.x>, <https://arxiv.org/abs/1009.4015> [astro-ph.CO]
- Spitzer L (1962) *Physics of Fully Ionized Gases*
- Stephens IW, Dunham MM, Myers PC, et al (2018) Mass Assembly of Stellar Systems and Their Evolution with the SMA (MASSES)—1.3 mm Subcompact Data Release. *ApJS*237(2):22. <https://doi.org/10.3847/1538-4365/aacda9>, <https://arxiv.org/abs/1806.07397> [astro-ph.GA]
- Syed J, Soler JD, Beuther H, et al (2022) The “Maggie” filament: Physical properties of a giant atomic cloud. *A&A*657:A1. <https://doi.org/10.1051/>

0004-6361/202141265, <https://arxiv.org/abs/2111.01057> [astro-ph.GA]

- Vázquez-Semadeni E, Palau A, Ballesteros-Paredes J, et al (2019) Global hierarchical collapse in molecular clouds. Towards a comprehensive scenario. *MNRAS*490(3):3061–3097. <https://doi.org/10.1093/mnras/stz2736>, <https://arxiv.org/abs/1903.11247> [astro-ph.GA]
- Villagran MA, Gazol A (2018) The influence of magnetic field on the cold neutral medium mass fraction and its alignment with density structures. *MNRAS*476(4):4932–4948. <https://doi.org/10.1093/mnras/sty438>, <https://arxiv.org/abs/1712.00466> [astro-ph.GA]
- West JL, Landecker TL, Gaensler BM, et al (2021) A Unified Model for the Fan Region and the North Polar Spur: A Bundle of Filaments in the Local Galaxy. *ApJ*923(1):58. <https://doi.org/10.3847/1538-4357/ac2ba2>, <https://arxiv.org/abs/2109.14720> [astro-ph.GA]
- West JL, Campbell JL, Bhaura P, et al (2022) Discovery of a Filamentary Synchrotron Structure Connected to the Coherent Magnetic Field in the Outer Galaxy. *ApJ*941(1):6. <https://doi.org/10.3847/1538-4357/ac9b58>, <https://arxiv.org/abs/2210.10098> [astro-ph.GA]
- Wolfire MG, McKee CF, Hollenbach D, et al (2003) Neutral Atomic Phases of the Interstellar Medium in the Galaxy. *ApJ*587(1):278–311. <https://doi.org/10.1086/368016>, <https://arxiv.org/abs/astro-ph/0207098> [astro-ph]
- Xu D, Kong S, Kaul A, et al (2023) CMR exploration II – filament identification with machine learning. arXiv e-prints arXiv:2308.06641. <https://doi.org/10.48550/arXiv.2308.06641>, <https://arxiv.org/abs/2308.06641> [astro-ph.GA]
- Xu S, Lazarian A, Yan H (2015) The Line Width Difference of Neutrals and Ions Induced by MHD Turbulence. *ApJ*810(1):44. <https://doi.org/10.1088/0004-637X/810/1/44>, <https://arxiv.org/abs/1412.8608> [astro-ph.GA]
- Xu S, Ji S, Lazarian A (2019) On the Formation of Density Filaments in the Turbulent Interstellar Medium. *ApJ*878(2):157. <https://doi.org/10.3847/1538-4357/ab21be>, <https://arxiv.org/abs/1905.06341> [astro-ph.GA]
- Yan H, Lazarian A (2002) Scattering of Cosmic Rays by Magnetohydrodynamic Interstellar Turbulence. *PRL*89(28):281102. <https://doi.org/10.1103/PhysRevLett.89.281102>, <https://arxiv.org/abs/astro-ph/0205285> [astro-ph]
- Yan H, Lazarian A (2004) Cosmic-Ray Scattering and Streaming in Compressible Magnetohydrodynamic Turbulence. *ApJ*614(2):757–769. <https://doi.org/10.1086/423733>, <https://arxiv.org/abs/astro-ph/0408172> [astro-ph]

- Yuen KH, Lazarian A (2017a) Tracing interstellar magnetic field using the velocity gradient technique in shock and self-gravitating media. arXiv e-prints arXiv:1703.03026. <https://arxiv.org/abs/1703.03026> [astro-ph.GA]
- Yuen KH, Lazarian A (2017b) Tracing Interstellar Magnetic Field Using Velocity Gradient Technique: Application to Atomic Hydrogen Data. *ApJL*837(2):L24. <https://doi.org/10.3847/2041-8213/aa6255>, <https://arxiv.org/abs/1701.07944> [astro-ph.GA]
- Yuen KH, Lazarian A (2020a) Advancing the Velocity Gradient Technique: Using Gradient Amplitudes and Handling Thermal Broadening. *ApJ*898(1):65. <https://doi.org/10.3847/1538-4357/ab9307>
- Yuen KH, Lazarian A (2020b) Curvature of Magnetic Field Lines in Compressible Magnetized Turbulence: Statistics, Magnetization Predictions, Gradient Curvature, Modes, and Self-gravitating Media. *ApJ*898(1):66. <https://doi.org/10.3847/1538-4357/ab9360>, <https://arxiv.org/abs/2002.01926> [astro-ph.GA]
- Yuen KH, Hu Y, Lazarian A, et al (2019) Comment on Clark et al. (2019) “The Physical Nature of Neutral Hydrogen Intensity Structure”. arXiv e-prints arXiv:1904.03173. <https://doi.org/10.48550/arXiv.1904.03173>, <https://arxiv.org/abs/1904.03173> [astro-ph.GA]
- Yuen KH, Ho KW, Lazarian A (2021) Technique for Separating Velocity and Density Contributions in Spectroscopic Data and Its Application to Studying Turbulence and Magnetic Fields. *ApJ*910(2):161. <https://doi.org/10.3847/1538-4357/abe4d4>, <https://arxiv.org/abs/2012.15776> [astro-ph.GA]
- Yuen KH, Ho KW, Law CY, et al (2022) *ApJL*, submitted, arXiv:220413760
- Yuen KH, Chen A, Ho KW, et al (2023a) The phase and turbulent properties of Cattail. *MNRAS*519(2):2701–2708. <https://doi.org/10.1093/mnras/stac3635>
- Yuen KH, Li H, Yan H (2023b) The origin and ubiquity of non-zero low-frequency fluctuations in Compressible Magnetohydrodynamic Turbulence. submitted
- Yuen KH, Yan H, Lazarian A (2023c) Anomalous compressible mode generation by global frame projections of pure Alfvén mode. *MNRAS*521(1):530–545. <https://doi.org/10.1093/mnras/stad287>, <https://arxiv.org/abs/2301.13344> [astro-ph.GA]
- Yusef-Zadeh F, Morris M, Chance D (1984) Large, highly organized radio structures near the galactic centre. *Nat*310(5978):557–561. <https://doi.org/10.1038/310557a0>

- Zhang GY, André P, Men'shchikov A, et al (2020a) Fragmentation of star-forming filaments in the X-shaped nebula of the California molecular cloud. *A&A*642:A76. <https://doi.org/10.1051/0004-6361/202037721>, <https://arxiv.org/abs/2002.05984> [astro-ph.SR]
- Zhang H, Chepurnov A, Yan H, et al (2020b) Identification of plasma modes in Galactic turbulence with synchrotron polarization. *Nature Astronomy* 4:1001–1008. <https://doi.org/10.1038/s41550-020-1093-4>, <https://arxiv.org/abs/1808.01913> [physics.plasm-ph]
- Zhao S, Yan H, Liu TZ, et al (2023a) Compressible Magnetohydrodynamic Turbulence Modulated by Collisionless Damping in Earth's Magnetosheath: Observation Matches Theory. arXiv e-prints arXiv:2305.12507. <https://doi.org/10.48550/arXiv.2305.12507>, <https://arxiv.org/abs/2305.12507> [astro-ph.SR]
- Zhao S, Yan H, Liu TZ, et al (2023b) Satellite Observations of the Alfvénic Transition from Weak to Strong Magnetohydrodynamic Turbulence. arXiv e-prints arXiv:2301.06709. <https://doi.org/10.48550/arXiv.2301.06709>, <https://arxiv.org/abs/2301.06709> [astro-ph.SR]
- Zweibel EG, Josafatsson K (1983) Hydromagnetic wave dissipation in molecular clouds. *ApJ*270:511–518. <https://doi.org/10.1086/161144>